

## Article

# Innovative Early Detection of High-Temperature Abuse of Prismatic Cells and Post-Abuse Degradation Analysis Using Pressure and External Fiber Bragg Grating Sensors

André Hebenbrock <sup>1,2,\*</sup>, Nury Orazov <sup>1</sup>, Ralf Benger <sup>1</sup>, Wolfgang Schade <sup>1,3</sup>, Ines Hauer <sup>1,4</sup> and Thomas Turek <sup>1,2</sup>

<sup>1</sup> Research Center Energy Storage Technologies, Clausthal University of Technology, Am Stollen 19A, 38640 Goslar, Germany

<sup>2</sup> Institute of Chemical and Electrochemical Process Engineering, Clausthal University of Technology, Leibnizstraße 17, 38678 Clausthal-Zellerfeld, Germany

<sup>3</sup> Fraunhofer Institute for Telecommunications, Heinrich Hertz Institute, Am Stollen 19H, 38640 Goslar, Germany

<sup>4</sup> Institute of Electrical Power Engineering and Electrical Energy Engineering, Clausthal University of Technology, Leibnizstraße 28, 38678 Clausthal-Zellerfeld, Germany

\* Correspondence: andre.hebenbrock@tu-clausthal.de

**Abstract:** The increasing adoption of lithium-ion battery cells in contemporary energy storage applications has raised concerns regarding their potential hazards. Ensuring the safety of compact and modern energy storage systems over their operational lifespans necessitates precise and dependable monitoring techniques. This research introduces a novel method for the cell-specific surveillance of prismatic lithium-ion cells, with a focus on detecting pressure increases through the surface application of a fiber Bragg grating (FBG) sensor on a rupture disc. Commercially available prismatic cells, commonly used in the automotive sector, are employed as test specimens and equipped with proven pressure and innovative FBG sensors. Encompassing the analysis capacity, internal resistance, and pressure (under elevated ambient temperatures of up to 120 °C), this investigation explores the thermal degradation effects. The applied FBG sensor on the rupture disc exhibits reversible and irreversible state changes in the cells, offering a highly sensitive and reliable monitoring solution for the early detection of abuse and post-abuse cell condition analysis. This innovative approach represents a practical implementation of fiber optic sensor technology that is designed for strain-based monitoring of prismatic lithium-ion cells, thereby enabling customized solutions through which to address safety challenges in prismatic cell applications. In alignment with the ongoing exploration of lithium-ion batteries, this research offers a customizable addition to battery monitoring and fault detection.



**Citation:** Hebenbrock, A.; Orazov, N.; Benger, R.; Schade, W.; Hauer, I.; Turek, T. Innovative Early Detection of High-Temperature Abuse of Prismatic Cells and Post-Abuse Degradation Analysis Using Pressure and External Fiber Bragg Grating Sensors. *Batteries* **2024**, *10*, 92. <https://doi.org/10.3390/batteries10030092>

Academic Editor: Mingyi Chen

Received: 15 January 2024

Revised: 23 February 2024

Accepted: 29 February 2024

Published: 4 March 2024



**Copyright:** © 2024 by the authors. Licensee MDPI, Basel, Switzerland. This article is an open access article distributed under the terms and conditions of the Creative Commons Attribution (CC BY) license (<https://creativecommons.org/licenses/by/4.0/>).

## 1. Introduction

The safety of lithium-ion battery technology in the context of battery electric vehicles and large-scale battery storage has become increasingly crucial as the market for large lithium-ion battery systems continues to grow [1,2]. Foremost of the demands on present battery systems arise from heightened energy density and rapid charging capabilities, necessitating robust safety measures in response [3]. However, achieving these goals is a complex task, with cost pressures and the need for more rigorous thermal management (owing to the rising energy density) challenging the design of safe battery systems [4,5]. Recent advancements have led to substantial improvements in understanding and addressing thermal runaway (TR) events within lithium-ion batteries. These include breakthroughs in replicating TR events [6–8], early detection methods for battery cell TR [9–14], strategies to

mitigate TR [15–17], and the prevention of thermal propagation [18]. From these ongoing advancements around the TR event ensue recommendations that translate to various regulatory levels [19,20]. Despite these improvements, there are still challenges in the field of early detection like the high computational effort required to extract accurate and relevant battery state data, as well as accounting for the development of relevant fault features due to the aging of the cell [5,14,21].

In recent years, various calorimetric studies have shed light on the reversible and irreversible degradation phenomena associated with thermal degradation in batteries leading up to a TR event, especially lithium-ion batteries using graphite-based anodes [22–24]. It has been proposed that the irreversible pressure increase observed during battery cell operation can be attributed to gas formation [25,26]. The nature and extent of gas-forming reactions in battery cells depend on factors such as temperature and the state of charge (SOC), which vary depending on the cell chemistry [18,27–30]. In addition to gas emission, the typical progression of TR inevitably leads to a significant increase in temperature [31]. The escalating cell pressure inexorably results in the opening of the battery cell, which is accompanied by a loud noise and visible smoke generation [32].

Therefore, leveraging the expansion of battery cells is one promising avenue for the early detection of battery degradation and critical battery states [33]. This volume increase can be utilized for cell state determination, early fault detection, and the identification of lithium plating in batteries [26,34,35]. Recent safety-related FBG application research in battery technology has particularly evolved based on strain measurements and internal sensing methods [35]. Complementary mechanical monitoring with fixed FBG sensors has proven to be particularly applicable in mechanically sensitive and lighter pouch cells [36], and it has also found applications in improved temperature sensing for inherently smaller cylindrical cells [37,38].

However, prismatic cells, commonly used as large format cells in various high-capacity systems, possess sturdy casings that make them less prone to expansion during operation compared to pouch cells, thereby limiting the usefulness of strain measurements. Additionally, lithium-ion battery cells are often externally braced in applications, further impeding the measurement of volume changes [34]. During operation, large format cells develop temperature fields that decrease in uniformity based on operational demand and cell size [39,40]. This is due to the small surface-to-volume ratio, which dampens cooling efficiency. Representative and system-wide temperature measurement is therefore challenging for larger cells.

This study introduces an innovative and non-invasive approach with FBG sensors for meaningful strain monitoring on commercial large format prismatic cells in a realistic braced application, thereby leveraging a mechanically fixed connection to the standard rupture disc in these cells for improved battery state determination. The experimental investigation targeting thermal abuse and internal gas evolution with parallel pressure measurement demonstrated the effectiveness of the FBG sensor application for sensitive strain measurements as an additional state parameter—complementary to voltage, current, and temperature—to ensure safe battery operation. Analysis of the underlying degradation reactions through phases of elevated temperatures of up to 120 °C revealed the potential for the early detection of critical pressures before a cell opening event. Thus, this work demonstrates a novel possibility for customizable and reliable cell-specific strain monitoring.

## 2. Materials and Methods

### 2.1. The Device under Test

The tested cell was an industry-standard, available prismatic cell of the PHEV2 type (according to the German Association of the Automotive Industry), and it was disassembled from a module with a nominal capacity of 37 Ah [41]. It was composed of nickel manganese cobalt oxide ( $\text{Li}_x \text{Ni}_{0.33} \text{Mn}_{0.33} \text{Co}_{0.33} \text{O}_2$ ) (NMC111)/graphite intercalation compound (GIC) chemistry, as well as polypropylene (PP) and polyethylene (PE) separator combination,

and it is usually employed in battery electric vehicle applications. Further relevant cell data from the manufacturer can be found in Table 1.

**Table 1.** Cell characteristics given by the manufacturer.

Property	Value
Mass/g	810
Length × width × thickness/mm	91 × 148 × 26.5
Upper cut-off voltage/V	4.2
Lower cut-off voltage/V	3.0
Maximum charge current/A	55
Maximum discharge current/A	123
Maximum storage temperature/°C	70
Minimum storage temperature/°C	-40
Maximum operating temperature/°C	60

Positioned in a symmetrically fastened arrangement, 8 mm thick aluminum plates clamped the cell on each side with a torque of 0.5 Nm. This applied torque resulted in a state-of-charge (SOC)-dependent pressure ranging from an approximate range of 0.074–0.11 MPa, which fell within the typical pressure range observed in automotive applications [42,43]. The cell was equipped with an overcharge safety device (OSD), which consisted of a pressure-sensitive aluminum diaphragm that causes an external short circuit when a certain pressure threshold is reached (Figure 1). The short-circuit current would cause the fuse to melt, which would interrupt the current flow [44]. Triggering the OSD would thus prevent further operation of the cell when an increased pressure is reached. To test the thermal degradation and to evaluate the effects on discharge capacity and internal resistance, the electrical operability must be preserved. The OSD was, therefore, deactivated beforehand by filling the membrane cavity with epoxy resin.

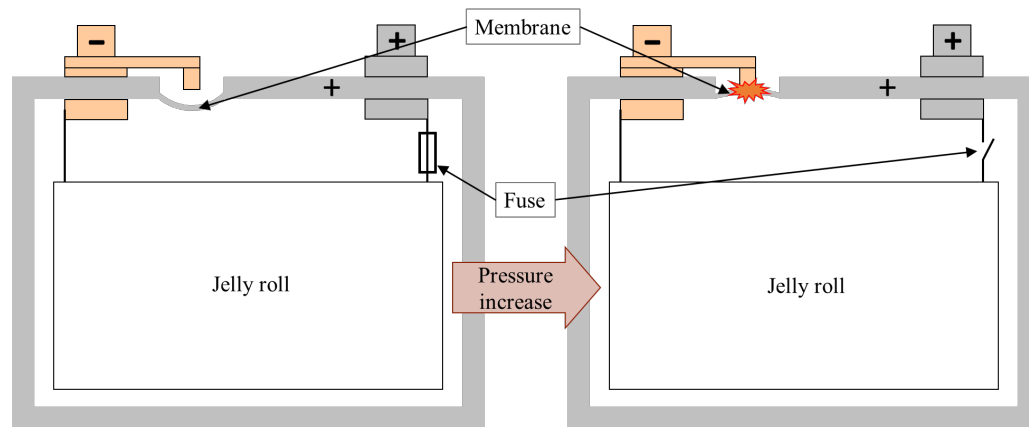


**Figure 1.** Schematic representation of the operation of the OSD in the prismatic cell showing the consequence of an external short circuit in the event of a pressure increase, as well as the subsequent triggering of the fuse. Based on ref. [44].

To allow for the cell opening to take place in a controlled way, the cell was equipped with a rupture disc as standard. The rupture disc was an approximately 0.15 mm thick aluminum sheet, and it was measured as 24 mm × 9 mm at its longest dimensions. It had a 12 mm-elongated perforation in the center. On both sides, two additional perforations protruded from it with a length of 4 mm at 135° (bottom left Figure 2).

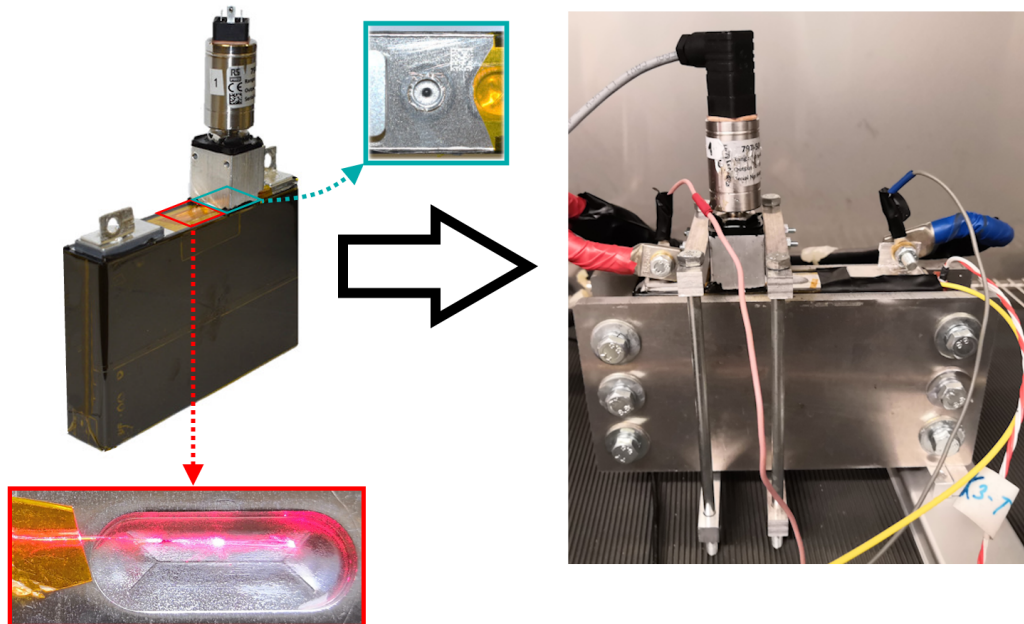


**Figure 2.** The cell was equipped with a pressure sensor (top left) and a fiber optic sensor (bottom left). The connection to the gas space was made by a penetration of the sealing pin. The sealing pin without the aluminum cover can be seen in the top middle breakout. The fiber optic sensor was positioned next to the elongated perforation and is marked by the red glowing dot in the middle. The clamped cell that was inside the climate chamber in the complete setup is shown on the right side.

## 2.2. Thermal Abuse Conditions

During the experiment, the cell was exposed to elevated ambient temperature phases in a 50–120 °C range. This high-temperature range was chosen to better quantify the less identifiable phenomena of cells overheating due to processes at the solid electrolyte interphase (SEI) layer of the GIC electrode. The test range, thus, started just below the maximum operating temperature, and it ended below the melting temperature of the PE layer in the separator, which would lead to pore closure, as well as drastic and thus easily identifiable irreversible degradation effects [31]. As for the used temperature range, we looked mostly at the reactions at the SEI layer on the graphite active material (Figure 3). The SEI layer is essential for the sustainable usage of lithium-ion batteries as a rechargeable energy storage, as the anode potential is otherwise outside the stability window of the electrolyte [45]. According to Peled et al. [46], the desired attributes are high electrical resistance, high selectivity, and low diffusion resistance for lithium-ion batteries, as well as low thickness, high mechanical stability against expansion, and a high tolerance for high temperatures and high potentials. The formation of the electrically insulating SEI layer started with the initial charging of a lithium-ion battery with a GIC anode to stabilize it against the potential window used. However, this SEI could not meet all the formulated requirements. With increased temperatures, electric cycling, and longer storage times, the layer thickness continued to increase [47].

The components of the initial SEI formation are composed of insoluble inorganic and partially soluble organic compounds like the reduction products of the electrolyte resulting from its reaction with lithium ions and electrons [46].

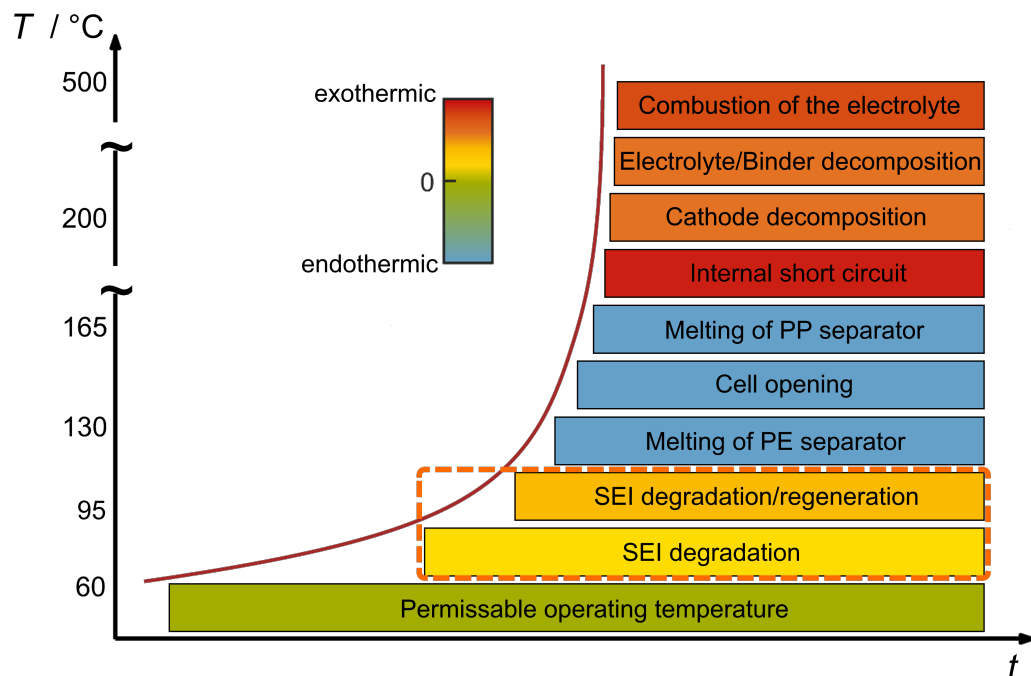
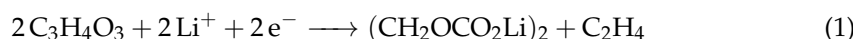
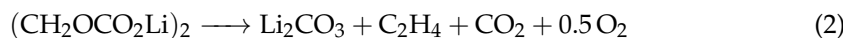


**Figure 3.** Progression of the cell events for the NMC/GIC chemistry and PE/PP separator with increasing temperature. Illustration style based on ref. [48] with insights from refs. [9,31,49].

The mix was strongly dependent on the solvent composition of the used additives and impurities [23]. The SEI formation reactions were irreversible and led to the binding of lithium ions, thereby contributing to capacity fade and Ohmic resistance increase (ORI) [22,47]. The exact electrolyte composition of the tested commercial cell is not known. Due to the similarity of the organic carbonate solvents commonly used in lithium-ion batteries, and for simplification in subsequent qualitative discussions, we assume the presence of EC. Consequently,  $(\text{CH}_2\text{OCO}_2\text{Li})_2$  emerges as the primary component in SEI formation, accompanied by the release of  $\text{C}_2\text{H}_4$ , as expressed in Equation (1) [50]:



The decomposition of the main component of the SEI can be described by the global reaction form at which the metastable  $(\text{CH}_2\text{OCO}_2\text{Li})_2$  reacts to the stable inorganic  $\text{Li}_2\text{CO}_3$ , as expressed in Equation (2) [51]. Furthermore, the reaction was shown to be largely independent of the lithium content of the anode [52]. The onset temperature of the decomposition reaction depends on the electrolyte composition [23,53]. Additionally, the initial heating rate/reaction rate was found to be greatly dependent on the graphite surface area [31]. Therefore, with the use of calorimetry, the starting temperature of the SEI degradation was found to vary in a range of 57–80 °C [52,53].



With increasing temperature, an acceleration in the decomposition of metastable SEI components to stable components can be assumed [31,52,54,55]. The SEI decomposition has a peak at roughly 100 °C. As shown by Richard and Dahn, the self-heating rate slows down but increases again as new SEI is formed if lithium ions are available in the GIC [52]. As in the initial SEI formation, all reactants (as expressed in Equation (1)) have to come in contact, which can be at the graphite/electrolyte or SEI/electrolyte interface and can lead to the increasing growth of the SEI layer even after complete coverage of the graphite [46]. These necessary reaction conditions for the reforming process are mainly managed by two mechanisms.

- Cracking of the SEI layer due to the expansion of the graphite during charging leads to direct contact of lithiated graphite with the electrolyte and thus to the reformation of metastable SEI [46,54].
- Since the SEI layer is conductive for lithium ions, and with the tunneling effect for electrons, a new metastable SEI layer can be formed on already existing inorganic SEI [52].

A parallel occurrence between SEI decomposition and formation could also be observed from about 100 °C by the calorimetry experiments [52,56]. This then led to an equilibrium in the reformation of metastable organic species being set externally over the inorganic SEI layer, which increasingly reacted to form the stable inorganic layer (Figure 4).

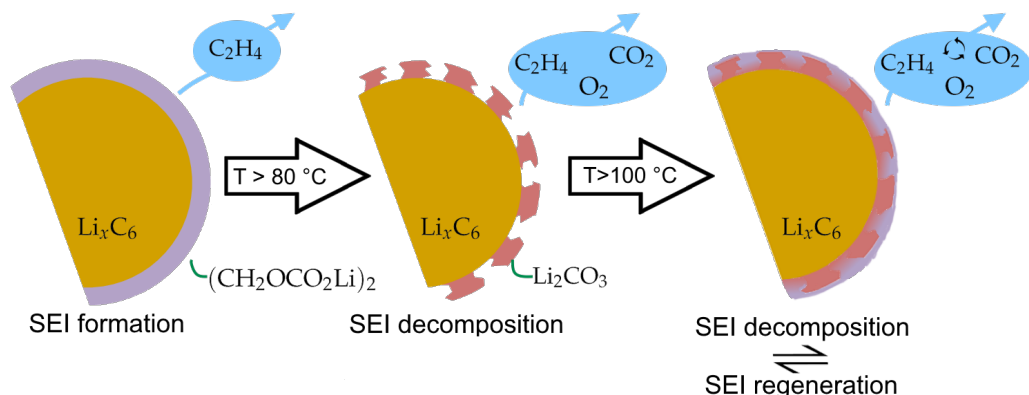


**Figure 4.** Schematic display of the temperature-dependent stages of the SEI composition and occurring reactions. Based on refs. [31,51].

At high temperatures, these reactions contribute to an irreversible growth of the stable SEI component ( $\text{Li}_2\text{CO}_3$ ), which passivizes the active material and thus increases the cell's resistance, as well as a deactivation of active anode regions [57]. Both the formation (Equation (1)) and the decomposition (Equation (2)) of the SEI layer are exothermic reactions which bind of lithium ions and lead to gas evolution [31,51]. When the emission of gases is compared (Equations (1) and (2)), it is obvious that significantly more gaseous species are released during the decomposition of the SEI layer, which shows that the measured pressure increase strongly depends on the onset of the decomposition.

### 2.3. Sensors

Battery cell degradation due to SEI growth during use manifests itself in changes in internal resistance and in the decrease in capacity due to loss of lithium inventory (LLI) and loss of active material (LAM) [58,59]. Depending on the use case, this leads to an unknown internal state and uncertain thermal stability [18]. To prevent the uncertainty conceptually, the examined prismatic cell was equipped with a pressure sensor and an FBG sensor on the rupture disc as a basis for the early detection and monitoring of the degradation progress.

#### 2.3.1. Pressure Sensor

In principle, a pressure sensor can be installed inside or outside the cell [60]. Here, an external cell sensor with a threaded connection was chosen for its simple installation. Despite its advantages, the sensor had some drawbacks, including dead volume and thermal mass, which were not considered in this work due to the large cell size (additional volume < 1% and mass < 0.5%). The selected piezoresistive ceramic sensor was suitable for use during the thermal loading of the cell, with a maximum storage temperature of 125 °C and a maximum media temperature of up to 135 °C. Exhibiting good media stability, the pressure sensor can measure pressures up to 6 bar relative to atmospheric pressure and provides an accuracy of  $\pm 0.25\%$ . Between the positive pole and the rupture disc, a welded-on protective cap on top of the sealing pin can be seen on the cell. After removing

the protective cap, there is an opening sealed with a plastic sealing pin, which is used during the production process to fill the cell with electrolyte (Figure 2). For attaching the sensor, an aluminum block with concentric inner threading was positioned over the sealing pin of the prismatic cell. Using this location for the measurement setup is considered advantageous due to the following reasons:

- It provides easy access to the opening without the need for drilling, which could introduce metal shavings into the cell and potentially cause an internal short circuit.
- Remaining uncovered, the rupture disc of the cell preserves its functionality, thus enabling the authentic behavior that is crucial to the FBG sensor.
- The electrolyte does not flow into the measurement block because of its position on top of the cell, thereby ensuring that the electrochemical properties of the cell remain unchanged.

For fixing the aluminum block, an adhesive silicon-based sealing paste (Acc Silicones—Part No.: 740010640) and epoxy resin (MG Chemicals—Part No.: 832HT-375ML) were utilized to bond the aluminum block to the cell housing. After hardening, the silicone-based adhesive sealing paste forms a resilient silicone elastomer and can withstand temperatures up to 300 °C. It was used as the outer ring sealant and the electric insulation between the aluminum block and the cell housing, which was connected to the positive pole.

An 8 mm-long tinned copper tube was fixed into the electrolyte pin opening with epoxy resin (maximum operating temperature of 200 °C) on the inside of the aluminum block. The chemical stability of the inner cured epoxy resin was tested by exposure to an electrolyte mixture of ethylene carbonate (EC):dimethyl carbonate (DMC) in a ratio of 1:1 with the conducting salt LiPF<sub>6</sub> in the concentration of 1 mol L<sup>-1</sup> and had shown no visible changes over 2 years.

Before the cell was opened by puncturing the seal pin's final plastic layer, the cell was transferred into an argon-filled glove box. As the final steps, the pressure sensor was mounted on the aluminum block together with the silicone O-ring seal (max. operating temperature 200 °C) inside the glove box, and it was cast on the outside with epoxy resin to ensure complete sealing. The successfully retrofitted sensor was braced against the cell and can be seen on the right side of Figure 2.

### 2.3.2. Fiber Bragg Grating Sensor

The fiber optic sensors used were single-mode 800 polyimide-coated glass fibers. In addition to their mechanical robustness and immunity to electromagnetic interference, these sensors have a small form factor. Inside this fiber are uniform FBGs inscribed by a femtosecond laser. Depending on the grating period  $\Lambda$  and the effective refractive index  $n_{\text{eff}}$ , the FBG reflects a specific Bragg wavelength ( $\lambda_B$ ), as can be seen in Equation (3) [61,62].

$$\lambda_B = 2\Lambda n_{\text{eff}} \quad (3)$$

These physical properties of the FBG grating are sensitive not only to mechanical strain, but also to temperature changes (Equation (4)) [61,62].

$$\frac{\Delta\lambda_B}{\lambda_B} = (1 - \rho_e)\Delta\varepsilon + (\alpha + \eta)\Delta T \quad (4)$$

The stress-optic coefficient  $\rho_e$ , the thermo-optic coefficient  $\eta$ , and the thermal expansion  $\alpha$  describe the effect of strain changes ( $\Delta\varepsilon$ ), as well as the temperature changes  $\Delta T$  on the Bragg wavelength when compared to the initial state of the measurement. The fiber optic sensor was mounted on the outside of the rupture disc parallel to the long perforation in the middle (bottom left Figure 2). This designed mechanical weakness as a safety feature is accessible, and it demonstrates the highest sensor sensitivity to state changes in the cell compared to other positions on the cell due to its thinness. Because of the orientation of the fiber on the rupture disc, the FBG was compressed with increasing swelling along the perforation as a result of the plastic deformation due to high cell pressure. After the irreversible

deformation, the FBG thus relaxed to a compressed state at reference conditions and was directly dependent on the degree of the increasing curvature, which led to a reduction in the grating period  $\Lambda$  and therefore to a decrease in  $\lambda_B$  (Equation (3)). This compression made it necessary to apply the fiber under tension during the application; otherwise, no measurement was possible [63]. To test for the highest sensitivity, a configuration with the sensor glued on one side and free on the other side along the elongated perforation (one-sided adhesive), which had an even distribution of the adhesive on both sides of the elongated perforation (balanced adhesive) for a more symmetrical deformation behavior, were tested (Figure 5).

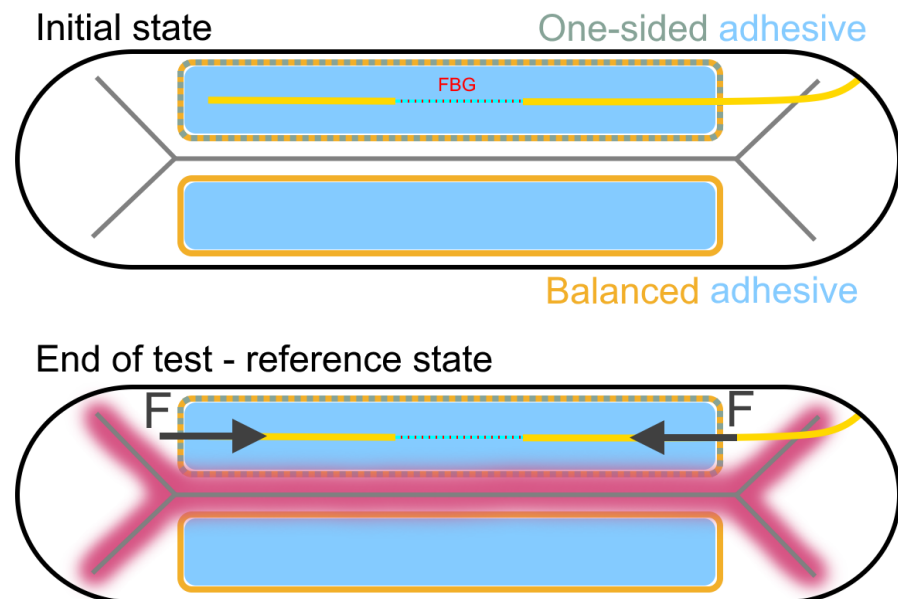


**Figure 5.** Scheme of transition from the initial state of the rupture disc to the state with swellings around the perforation at 25 °C after the thermal abuse test (red). In the one-sided configuration, only the area around the FBG sensor was glued to the rupture disc (gray box). In the balanced configuration (yellow boxes), both sides of the elongated perforation were glued for a more symmetric deformation.

To optimize the strain transfer, the fiber was bonded with a cyanoacrylate-based adhesive (Loctite 406) with a high Young modulus for optimal strain transfer (which was stable up to 120 °C and parallel to the center perforation with low adhesive thickness between the bursting disc and fiber). The bond length was chosen to be as long as the elongated perforation. To further improve the strain transfer of the FBG sensor, the polyimide coating was removed from the fiber [63,64]. Before the adhesive was used, the surface was roughened with 80-grit abrasive paper, which was then afterward cleaned with isopropyl alcohol. The bonding process took place in two steps. First, the tip of the sensor was glued next to the end of the elongated perforation that was midway to the wall of the rupture disc. This was followed by bonding the remaining fiber to the aluminum next to the perforation under tension. Using this two-step method allowed for the application of sufficient pretension to the fiber so as to allow the measurement of the increasing compression. For the balanced glue configuration, the other side of the long perforation was also coated with the same amount of adhesive to ensure the symmetrical behavior of the rupture disc's deformation. In addition to the rupture disc's surface-applied FBG sensor, there was an additional FBG sensor in a 3 cm distance along the fiber, which was attached loosely to the cell with a narrow adhesive strip that was perpendicular to the fiber course. This free FBG sensor served as a temperature reference to the bonded FBG sensor and was mechanically decoupled from the cell.

## 2.4. Experimental Method

In Figure 6a, it can be seen that the clamped cell in the climate chamber was electrically connected to an electric battery test rig (Scienlab-SL60/200/12BT4C, Bochum, Germany), which controls the electrical load; supports the galvanostatic electrochemical impedance spectroscopy (GEIS) that operates in a frequency range of 10 mHz to 5 kHz and a maximum current amplitude of 5 A, as well as logs the pressure sensor, the cell temperature by a Pt100 sensor on top of the cell, the chamber temperature, current, and voltage of the cell. Additionally, the fiber with the FBGs was monitored by a commercial FBG measurement system (FiSens-X400, Braunschweig, Germany). Each adhesive configuration on the rupture disc was tested two times (balanced: B1 and B2 and one-sided: O1 and O2). Overall, the measurement frequency was 1 Hz. The pressure and free FBG measurement was performed only for the B1 and O1 configurations due to the high similarity of the measurement results.

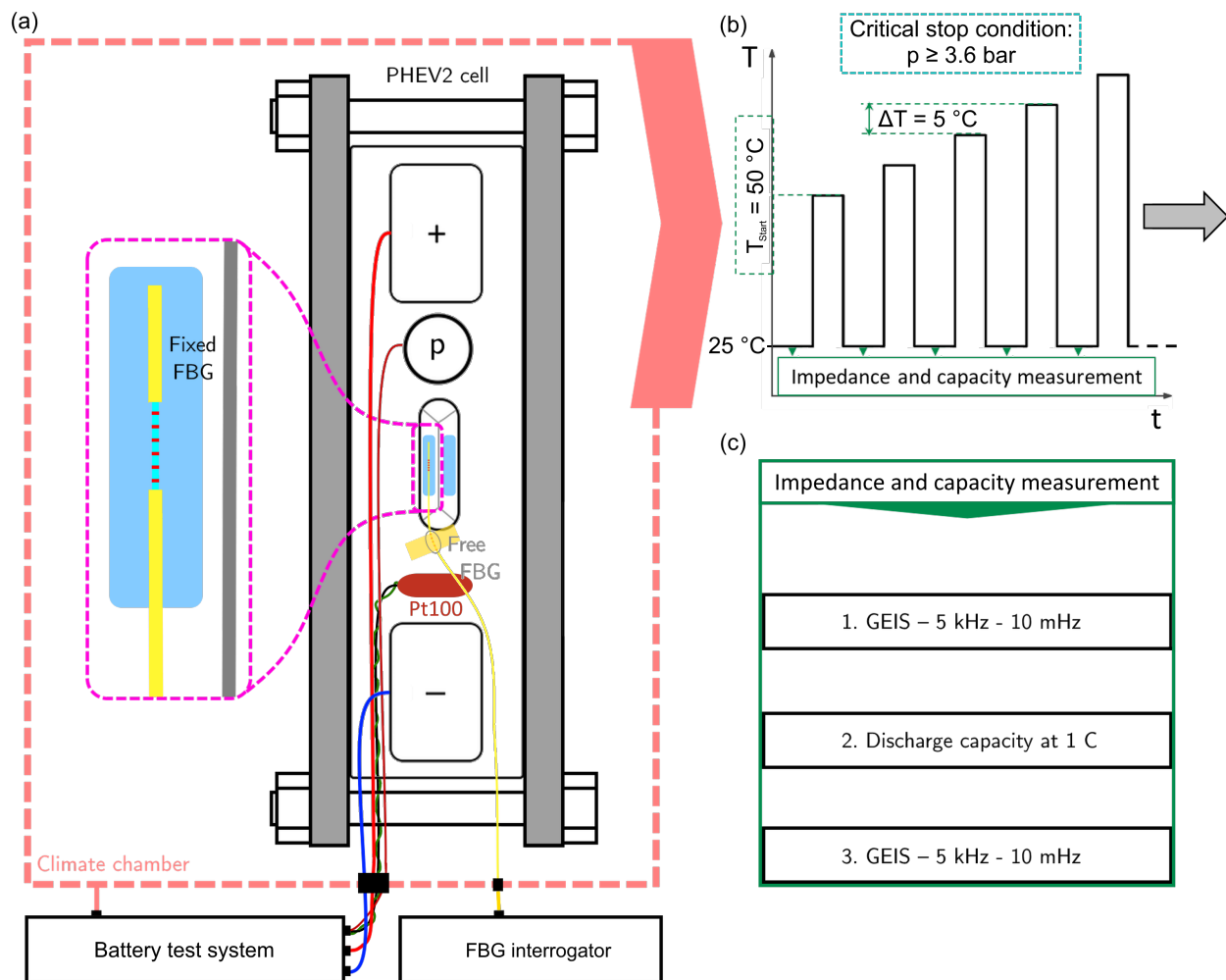


**Figure 6.** (a): Test setup of the prismatic PHEV2 cell used in the experiment with a pressure sensor and FBG sensor in the balanced configuration. (b): Gradual temperature increase in 5 °C steps from a range pf 50–120 °C or until a measured pressure of 3.6 bar was reached. (c): The electrical characterization procedure during the reference temperature phases after a 3 h relaxation at 3.95 V.

A climate chamber (Binder-MK720) with a heating rate of  $4 \text{ K min}^{-1}$  and a cooling rate of  $4.5 \text{ K min}^{-1}$  was chosen to minimize the transition times between each phase. To ensure the safety of the test, the experiments were carried out in a safe environment with a set critical pressure limit that was determined beforehand by heating an identical cell until the rupture disc burst. The critical pressure limit until test termination was set to 3.6 bar. To investigate the increasing thermal degradation effects of the cell, a sequence of reference and

high-temperature phases going from a range of 50–120 °C in 5 °C increments were applied to the cell (Figure 6b). The test was finished when the 120 °C high-temperature phase was concluded, or it was ended prematurely when the critical pressure limit was reached.

After each 3 h high-temperature phase, the cell was electrically characterized during a 20 h-long reference temperature phase at 25 °C by a procedure comprising a GEIS before and after a capacity test to monitor the change in cell impedance after every high-temperature phase (Figure 6c). The complete electrical procedure from the start of the cooling from a high-temperature phase to the start of the next is listed below. There were two cells in the climate chamber for each experiment. Steps 2 and 3, as well as 6 and 7, were swapped for the cells in the O1 and O2 configuration to perform GEIS on only one cell at a time, thereby avoiding interference.

1. Hold voltage at 3.95 V for 4 h once the reference temperature of 25 °C is reached;
2. GEIS at 5 A from 5 kHz to 10 mHz for 10 sine periods;
3. Rest 1 h;
4. Capacity check at 1 C (2×)
  - (a) Discharge at 1 C until 3 V;
  - (b) Rest 1 h;
  - (c) Charge at 1 C until 4.2 V;
  - (d) Hold voltage 4.2 V until C-rate drops to 0.05 C;
  - (e) Rest 1 h.
5. Discharge at 1 C to the desired 80% SOC;
6. Rest 1 h;
7. GEIS at 5 A from 5 kHz to 10 mHz for 10 sine periods;
8. Hold voltage at 3.95 V during the next high-temperature phase.

Before the start of the abuse test, the SOC of the cell was charged to 100% by a 1 C constant current (CC) charge and a 4.2 V constant voltage (CV) phase; this phase ended when the current dropped to 0.05 C, and it was then set to 80% SOC by a 1 C CC discharge phase. The cell was held at a constant 3.95 V (80% SOC) during the high-temperature phase to keep the boundary conditions for the SEI reactions constant. Thus, the experiments were conducted at a higher SOC close to the upper operation limit of commercially used cells [65]. Increasing the SOC any further would result in intensified gas emissions due to higher cell voltage, which are not related to the degradation phenomena under investigation [30]. After the end of the abuse test, the cells were cycled two times at 20 °C and in a CC phase at 0.05 C. These measured voltage responses were used for incremental capacity analysis (ICA) and were compared against cells without thermal abuse (Section 3.2).

### 3. Results and Discussion

All the temperature abuse tests were finished within a complete temperature range of 50–120 °C (Table 2). The overview of the capacity fade, ORI, maximum pressure increase (only B1 and O1), as well as the maximum FBG wavelength change compared to before the abuse, can be seen in Table 2. The capacity fade after the experiment was approximately 6% of the initial capacity. The resistance increases were around 25% except for the test O2, which had shown a problem with the GEIS measurement. A maximum pressure of 3.4 bar was reached during the 120 °C phase for the B1 and O1 tests. The start-to-end change in the wavelength change (at 1 Hz with an accuracy of  $\pm 2$  pm) of each fixed FBG adhesive configuration was spread from a 0.74–1.20 nm range, thereby showing that there was potential for improving the quality of application methodology to reach more consistent results. The trends of all the tabulated characteristics over the thermal abuse can be seen in Appendix A.2.

**Table 2.** Degradation overview of the capacity fade, FBG wavelength change at reference conditions, pressure, and ORI after completion of the thermal abuse test. Additionally, the temperature-specific wavelength change of the fixed FBG sensors at 50 °C are displayed.

Property	Value			
ID	O1	O2	B1	B2
Max pressure/bar	3.40	-	3.44	-
FBG hub/nm	-1.02	-0.74	-0.86	-1.20
Capacity decrease/%	5.32	6.15	5.00	7.09
ORI/%	26.29	134.92	26.77	27.45
$\Delta\lambda_{fix}/\Delta T/\text{pm K}^{-1}$ —before until end of 50 °C phase	21.2	19.1	13.2	18.4
$\Delta\lambda_{fix}/\Delta T/\text{pm K}^{-1}$ —cycle after 50 °C phase	36.8	43.4	37.4	36.1

### 3.1. State Development during Thermal Degradation

The test performance of the conducted tests proceeded in a very similar fashion. The following describes the results of experiment B1. It can be seen in Figure 7a that, in each phase of increased temperature, the wavelength change of the free FBG sensor was found to be directly proportional to the cell temperature. By comparison, the reversibility of the Bragg wavelength of the fixed FBG was equal to the free FBG up to the maximum storage temperature of 70 °C (Figure 7b). Thus, up to this temperature, the deformations of the rupture disc were exclusively elastic. Exceeding this temperature led to a plastic bulging in the perforations on the rupture disc during the high-temperature phase, which was shown as an irreversible wavelength decrease due to the resulting compression of the fixed FBG in the following phase at reference temperature. However, like the free FBG, the relative signal change of the fixed FBG can be directly correlated with the temperature rise during the high-temperature phase, thereby allowing for temperature monitoring. While the sensitivity for the free FBG was based on the thermal part of Equation (4), and showed an effective sensitivity of 8 pm K<sup>-1</sup>, the sensitivity of the fixed FBG during the high-temperature phase was three times higher (Table 2). As the complete fiber was assumed to be at an ambient temperature, the additional wavelength shift could be attributed to the thermal expansion of the host material. In contrast to the increasingly visible irreversible changes in the FBG that were fixed on the thin rupture disc, the expansion-induced higher temperature sensitivity could also be shown for other fixed FBG measuring points on the robust aluminum housing of the prismatic cell in the preliminary experiments.

Before starting the experiment, the pressure at the reference conditions inside the cell was at a slight over-pressure at a constant 160 mbar (Figure 7b). The pressure exhibited purely reversible pressure increases due to thermal expansions up to 75 °C. An irreversible pressure rise became apparent within the following high-temperature phases. In the closed cell, the increase in pressure at reference conditions could only be related to the gas evolution inside the cell due to the onset of the SEI degradation reactions. These irreversible contributions of both the pressure and the fixed FBG sensor were superimposed with the thermal expansion at elevated temperatures. As the deformation state was directly dependent on the cell pressure due to the design of the rupture disc, the measurable compression of the fixed FBG was found to be dependent upon the significantly larger pressure increase from the thermal expansion rather than the additional gas generation.

In addition to the increasing irreversible changes in the sensor signals, the GEIS performed also showed an ORI of the cell. The repeated GEIS measurements at 80% SOC and at the reference conditions showed a high reproducibility between the measurements before and after the determination of the discharge capacity. Therefore, only the first impedance spectrum after the high-temperature phases at 50, 85, and 120 °C can be seen in Figure 7c. The GEIS measurements showed an ORI leading to a shift along the real-axis in the characteristic impedance spectrum (at 50 °C) that saw increasing temperature.

In Figure 7d, the current ( $I < 0$  is a discharge) of the capacity measurement with two discharge cycles at 1 C is shown at 50 °C. The second discharge  $\Delta Q_{dis,2}$  was used as a

reference for capacity determination. With the measurement after 50 °C taken as a reference measurement with 38.82 Ah, the discharge capacity decreased to 36.89 Ah after the 120 °C phase. On the secondary axis of this plot, the measured temperature of the Pt100 sensor on top of the cell showed a temperature increase of 1.5 °C at the end of the discharge phase.

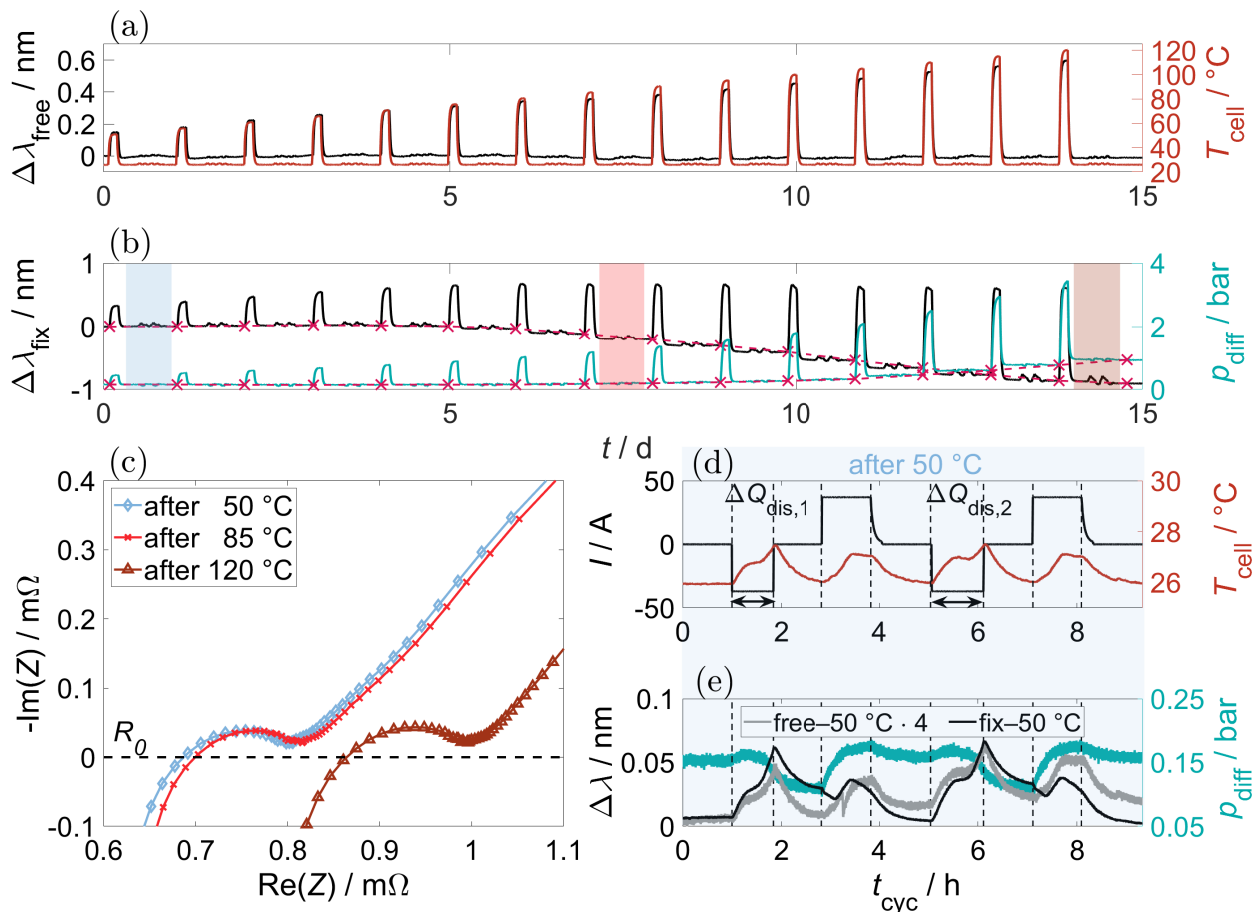


**Figure 7.** Overview of the results of experiment B1. (a): The free FBG wavelength change and temperature profile of the Pt100 sensor on top of the cell during test time. (b): Progression of the pressure and fixed FBG signals over the test duration and high-temperature phases that saw initial reversible changes up to 70 °C and which accumulated irreversible changes with increasing temperature. (c): Impedance spectroscopy spectra after 50, 85, and 120 °C temperature phases before capacity determination at 25 °C. (d): Current profile for the capacity determination and measured temperature at 25 °C after the 50 °C phase. (e): Sensor performance of the pressure, as well as the free and fixed FBG sensor during cycling after 50 °C. The wavelength change of the free FBG sensor was multiplied by four to create a comparable signal level to the fixed FBG sensor.

The cyclic load with changes in the SOC, which led to minimal cell temperature increase, was particularly interesting for the applied sensors to test their sensitivity during normal operation at the constant ambient temperature of 25 °C. Therefore, the optical wavelength shift of the fixed and free FBG sensor and the pressure, which were obtained during the same procedure, are displayed in Figure 7e. While dependent on the gas temperature inside the cell, the equilibrium pressure was directly proportional to the SOC of the cell, which can be seen during the relaxation phases in between the charge and discharge phases. This was in line with other results found in the literature, and it can be explained by the different states of the volumetric expansion of the electrodes depending on the SOC [66,67].

Looking at the FBGs, the results for the free FBG were corrected accordingly in the plot to allow for a comparison of trends (Figure 7e). The direct proportionality of the

free FBG to the temperature profile became less accurate during cycling due to the low sensitivity. In addition, between hours 3 and 4, there was a steep decrease in  $\lambda_B$ . This irregular effect can be observed on average 2 to 3 times a day, and it was related to the mechanical disturbances outside the described test environment that were due to other activities in the lab environment to which the free FBGs sensors were susceptible.

The temperature profile was captured more precisely by the fixed FBG sensor as it displays a sensitivity over  $35 \text{ pm K}^{-1}$  (Table 2), which was averaged by the temperature difference at  $150 \text{ mbar} \pm 10 \text{ mbar}$  during the discharge between hours 1 and 2, as well as 5 and 6 (Figure 7e). By comparing the sensitivity of the fixed sensor during the high-temperature phase and cycling, it became evident that the pressure increase led to a compression in the FBG (Table 2). This became especially apparent when we compared the sensitivities to the temperature during cycling with small pressure changes of  $\approx 70 \text{ mbar}$  and the  $50 \text{ }^\circ\text{C}$  phase with increased pressures at  $\approx 270 \text{ mbar}$  in Table 2. The apparent sensitivity to even minor pressure changes in the performed tests could be seen at the start of the charge phase for cell B1 (just after hours 3 and 7), where the charge led to a steep increase in pressure due to the parallel temperature and SOC increase. During the start of the charge, it could thus be seen that the fixed FBG signal decreased despite the increase in temperature. Later, during the charge, the pressure gradient decreased, which led to an increase in Bragg wavelength until the temperature reached a constant of  $27 \text{ }^\circ\text{C}$ . Overall, the fixed FBG sensitivity to temperature predominated due to the thermal expansion of the material, while the SOC dependency was only noticeable under certain conditions due to the minimal changes in pressure in the SOC range.

The small elastic geometry changes of the rupture disc leading to the elastic compression of the fiber show an increasing wavelength change after the completion of the test due to an increase in the sensitivity of 30–80% at the last cycle depending on the test (Figure 7b). The sensitivity toward these small pressure changes seemed to vary between each test and was most likely highly susceptible to minor changes in the fiber positioning and adhesive geometry on the whole rupture disc.

A lower sensitivity toward pressure changes and a more direct proportionality of the fixed FBG to the temperatures during these cycling conditions can be seen in the analog figures of the experiments O1 (Figure A1), B2 (Figure A2), and O2 (Figure A3).

The development of the start-to-end normalized state changes of pressure, ORI, and capacity at reference conditions before the start of the next high-temperature phase showed an exponential deterioration over the intensified thermal abuse (Figure 8). The normalized measurement profiles of the irreversible wavelength changes in the first experimental test, which exemplified the differences in the fixed FBG adhesive configurations, are also depicted in this figure. These profiles did not exhibit an exponential dependence on the temperature level of the preceding phase.

After each high-temperature phase, there was an increasing change in the Ohmic resistance and discharge capacity (Figures A4 and A5). However, the irreversible rise of pressure only started after the high-temperature phase at  $75 \text{ }^\circ\text{C}$  (Figure A6). Reaching the onset temperature of the SEI decomposition led to gas emissions that increased exponentially with increasing temperatures due to the decomposition reaction rate (Figure 8) [51]. This was also consistent with the measurable plastic deformation of the rupture disc by the fiber optic sensor system after the high-temperature step in the setup, which was conducted with a balanced distribution of adhesive on both sides of the middle perforation. However, this did not develop exponentially but correlated linearly in a range of  $75\text{--}115 \text{ }^\circ\text{C}$  for B1 and a range of  $85\text{--}115 \text{ }^\circ\text{C}$  for B2, which saw increasing temperatures in the high-temperature phases (Figure A7).

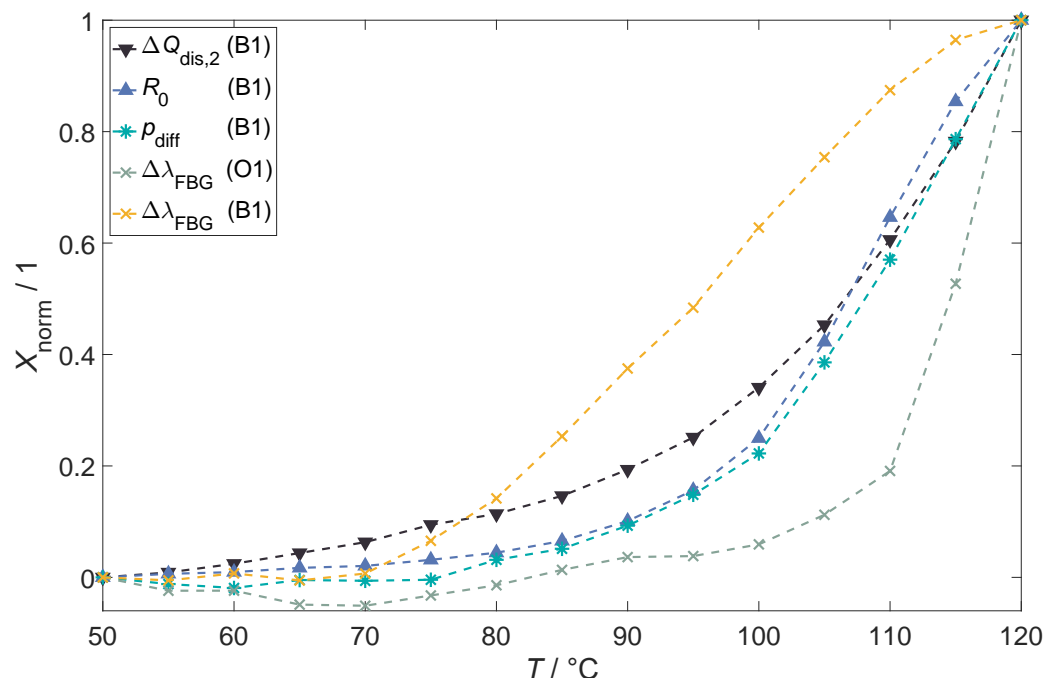


**Figure 8.** Progression start-end that was normalized in terms of the discharge capacity fade, ORI, pressure increase, and Bragg wavelength decrease in the fixed FBG, which was configured with an adhesive applied to one side (O), as well as both of the sides (B) of the middle rupture disc perforation after each high-temperature phase at 25 °C.

Because of the designed structural weakness to a plastic deformation of the aluminum rupture disc, the FBG sensor used here showed a clearer signal change compared to the pressure sensor. As the pressure approached the critical pressure limit, the linearity of the decline in the relaxed wavelength change decreased. This is an indication that the tensile strength of the aluminum of the bulging rupture disc had been reached and that the mechanical failure of the rupture disc had begun. Due to its direct dependence on the internal pressure, the deviation from linearity was a good indicator of the coming failure of the rupture disc, which thus enabled reactions to be made. Therefore, the early detection of critical rupture disc deformations due to critical pressure developments was directly enabled by monitoring the intentionally weakest point of the cell housing.

In contrast, the results of the one-sided configuration exhibited no reproducibility in the  $\lambda_B$  change during the high-temperature abuse. Particularly striking was, before the period of the expected decrease in the  $\lambda_B$  after 110 °C, the increase in wavelength in the O2 configuration. A positive wavelength change indicates an elongation. This can be explained by the non-parallel fixation of the FBG sensor near the center perforation, whose increasing curvature on the side of the FBG sensor explained the increase in  $\lambda_B$  from a range of 90–110 °C (Figure A7). When increasing the pressure, depending on the adhesive geometry on the rupture disc, there were variations in the extent of deformation. The use of a symmetric adhesive geometry resulted in a more homogeneous resistance behavior against deformation on the rupture disc. This led to a balanced configuration on the sensor side detecting (linear) changes significantly earlier. On the other hand, in the one-sided configuration, the adhesive-reinforced side, along with the sensor perforation, caused a higher mechanical resistance on the sensor side, thus resulting in lower sensitivity to pressure changes.

Thus, the sensor in the one-sided configuration effectively showed a less significant signal at slightly elevated temperatures, as well as drastic increases in the plastic deformation above 110 °C (Figure 8). The non-linearity and lower signal expression of this application alternative thus reduced the easily accessible informative value for state detection.

### 3.2. Incremental Capacity Analysis

Due to the good suitability of the ICA for the investigation of various significant degradation phenomena like the loss of mobile lithium inventory (LLI), loss of active material (LAM), and changes in ORI, the change in incremental capacity ( $dQ/dU$ ) due to the thermal abuse test of the damaged cells was considered [59,68]. To evaluate the degradation effects, the results of the two cycles at a current rate of 0.05 C at a 20 °C ambient temperature on the cells after the high-temperature step test, as well as two undamaged cells, were compared to each other. Before the determination of the incremental capacity of each of these cells, the final charge and discharge curve of the voltage was smoothed with a Gaussian filter for a window of 400 s to improve the curve feature visibility. Figure 9 shows the  $dQ/dU$  curves of the undamaged cells, as well as the B1 and O1 cells as a function of the cell voltage for charge ( $dQ/dU > 0$ ) and discharge ( $dQ/dU < 0$ ).

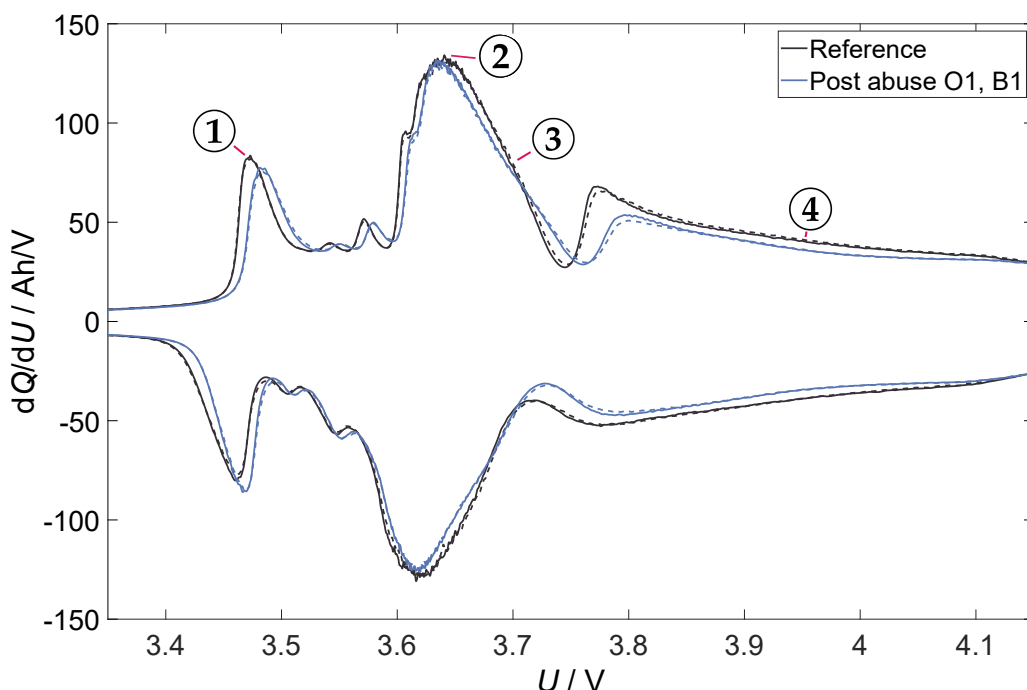


**Figure 9.** Incremental capacity analysis of the two reference cells without thermal degradation and the two cells after the thermal abuse test (B1 and O1) at a constant SOC of 80% during charge ( $dQ/dU > 0$ ) and discharge ( $dQ/dU < 0$ ). The features of interest during the charge phase are annotated by ① to ④.

The incremental capacity curves of the damaged cells and the reference cells showed good agreement, which indicates good cell quality and high reproducibility in the thermal step tests concerning the degradation state. Significant features of interest (FOI) for the NMC111/GIC cell chemistry are shown in Figure 9 by ① to ④. These FOI enabled assessments of the degradation phenomena [59]. Each feature was a combination of the electrochemical reactions at the positive and negative electrodes depending on the material [68]. The peaks identifiable in the NMC111/GIC results are largely dependent on the graphite [59,68,69]. There are further smaller peaks that are identifiable; these have been, however, disregarded due to their uncertain meaning [59]. Due to the oversized capacity for lithium ions after formation, the LAM was only detectable with a delay (incubation time) [58,59,70]. Any LAM may, therefore, be masked by the LLI accordingly [58,70].

For the NMC111/GIC chemistry, the effects can be interpreted according to Table 3, which lists the individual contributions of delithiated LAM (deNMC111 and deGIC), lithiated LAM (liNMC111 and liGIC), LLI, and ORI that have been studied by Dubarry et al. [59].

**Table 3.** Interpretation of the prominent feature shift of the NMC111/GIC cell chemistry due to different degradation effects. Multiple arrows correspond to the multiple positions that are dependent on the progression of degradation. The table is based on degradation maps for NMC111/GIC [59].

Property	①	②	③	④
LLI	→	↘	=	= ↘↗
LAM <sub>deNMC111</sub>	← ↖	↖	↖↗	↓
LAM <sub>LiNMC111</sub>	↘	↓	=	↓
LAM <sub>deGIC</sub>	=	=	↖↗	= ↘↗
LAM <sub>LiGIC</sub>	→	↘	=	= ↘↗
ORI	→	→	→	→

The increase in the ORI by about 25% led to no constant shifts in the peaks in the charging or discharging directions to higher or lower potentials, respectively (Figure 9), which quantitatively corresponded to the degradation map by Dubarry et al. [59]. The shift of the feature ① for the NMC111/GIC material system was found to be suitable for determining whether the positive electrode was limiting. In this case, the peak would shift to the left (←) until it disappeared (↖) [59]. A shift to ↘ was observed at ①, this corresponded to the LLI, which would include the loss of lithiated active material (LAM<sub>LiGIC</sub> and/or LAM<sub>LiNMC111</sub>) and could not be distinguished in this full cell ICA (Table 3). However, due to the continuous SEI formation, the LLI can be assumed in that case. Feature ③ (=) fits the degradation mode while ④ (↓) remains rather inconclusive as the position of this feature varies a great deal depending on the progression of the LLI [59]. Interestingly, feature ② showed only the slightest decrease in potential and incremental capacity, and it was found to be unusually independent of the combination of degradation phenomena compared to the other literature data [58,59]. Overall, the ICA supported the LLI and showed no detectable LAM that corresponded to the expected degradation phenomena in this temperature range (Figure 3).

### 3.3. Pre-Critical Thermal Abuse Correlations

When the onset of the irreversible pressure increase was examined, the exothermic decomposition of the SEI layer began after the 80 °C phase (Figure A6). The ensuing reformation reactions of the SEI layer contributed to an irreversible growth in the stable SEI components. Subsequent increments in temperature beyond 100 °C did not result in a further acceleration of the SEI layer decomposition and reformation, and this was evident through a linearization that commenced from this temperature phase during pressure rise, as depicted in Figure A6. This behavior, indicative of the kinetic limitations on the involved reactions, aligns with documented evidence in the literature [31]. This limited reaction equilibrium binds an increasing number of lithium ions and further passivates the GIC. The resulting SEI recomposition causes—in addition to the irreversible pressure increase due to gas evolution (as expressed by Equations (1) and (2))—increasing ORI (Figure 7b) and LLI, as shown by the ICA (Figure 9), which is also reflected in the increasing loss of capacity. As these effects are based on the same reactions at the tested temperature range, a strong correlation between them can be shown (Figure 8). The wavelength shift of the FBG sensor on the rupture disc at reference conditions was directly dependent on the plastic deformations on the rupture disc. In comparing the one-sided and balanced configuration, it was found that the development of the plastic deformations was strongly dependent on the glue distribution and correlates with the maximum pressure, which is a result of thermal expansion during the high-temperature phase. Therefore, it was not directly connected to the changes in the SEI layer composition. For the balanced configuration, the linear correlation to the reversible pressure increase was preserved due to the symmetric deformation behavior of the rupture disc. In the one-sided configuration, the plastic deformations of the glue-reinforced rupture disc side were only unambiguous at temperatures over 110 °C. The correlation of the degradation phenomena in the pre-critical thermal abuse can be summarized as shown in Figure 10.

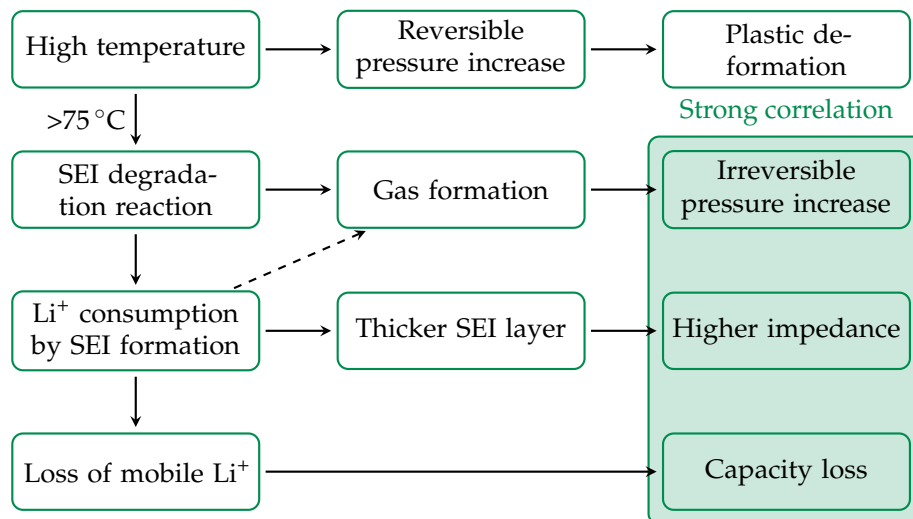


**Figure 10.** Correlation map of the degradation phenomena due to irreversible changes in measurable cell characteristics with an onset of SEI decomposition due to measurable gas formation over 75 °C.

#### 4. Conclusions

Analysis of the experimental results showed that exceeding the maximum storage temperature during high-temperature phases contributes to the expected recomposition of the SEI layer, thus leading to increasing passivation (ORI), irreversible pressure increase, and capacity fade due to LLI, which was shown by ICA. The presented instrumentation of the standard rupture disc by fixed FBG sensors was shown to be reliable up to a temperature of 120 °C in terms of allowing temperature and rupture disc deformation surveillance.

A one-sided and balanced configuration of glue was tested for the FBG fixation. The balanced adhesive configuration displayed optimal conditions for a cell-specific, combined sensitive temperature sensor, as well as for reliable rupture disc monitoring due to the linear trend for plastic deformation that was shown. In contrast, the one-sided configuration failed to present a reproducible trend and unambiguous progression toward critical pressures. This showed the individual optimization potential for monitoring solutions, which depends on the exact location and application of the fixed FBG sensor.

The key features displayed by the fixed FBG sensor during these thermal abuse experiments were as follows:

- On the rupture disc, the fixed FBG sensors showed highly sensitive proportionality to temperature, as well as an inverse proportionality to the cell pressure.
- The fixed FBG application displayed regardless of the adhesive configuration sufficient sensitivity for cell temperature monitoring, and it also showed potential for the in operando detection of critical cell states.
- The direct correlation of the plastic deformations to the pressure via the mechanical properties of the rupture disc allowed for the determination of cell-specific critical states within a battery system, as well as ensured early warnings for the cell rupture event.

These sensor properties, thus, showed a robust baseline as a sensor in both normal operation and critical stress. Therefore, they also showed a feasible extension with favorable properties such as the small form factor and reliability in the monitoring of large format prismatic cells. However, it is important to investigate the potential for the early fault detection of developing local defects in large format prismatic cells with the proposed concept to establish a minimal severity in developing cell faults in future work.

**Author Contributions:** Conceptualization, A.H. and N.O.; methodology, A.H. and N.O.; software, A.H.; validation, A.H. and N.O.; formal analysis, A.H.; investigation, A.H. and N.O.; resources, T.T., R.B. and W.S.; data curation, A.H.; writing—original draft preparation, A.H.; writing—review and editing, A.H., N.O. and T.T.; visualization, A.H.; supervision, R.B., I.H. and T.T.; project administration, R.B.; funding acquisition, R.B. and T.T. All authors have read and agreed to the published version of the manuscript.

**Funding:** Parts of this research were conducted within the Research Training Group CircularLIB, which was supported by the Ministry of Science and Culture of Lower Saxony, with funds from the program zukunft.niedersachsen of the Volkswagen Foundation. Parts of this research were also funded by the Federal Ministry for Economic Affairs and Energy of Germany in the project RiskBatt (project number: 03EI3010A). Other parts were funded by the Federal Ministry of Education and Research of Germany in the project VentBatt (project number: 03XP0535A).

**Data Availability Statement:** The data supporting the findings of this study are openly available on Zenodo, a trusted open-access repository. The datasets associated with this research can be accessed at the following doi link: [10.5281/zenodo.10262033](https://doi.org/10.5281/zenodo.10262033). The provided data include the raw optical, thermal, and electrical values for the abuse test, as well as ICA data, which allowed for the reproducibility and verification of the results presented in this manuscript. Researchers, readers, and interested parties are encouraged to access and utilize the provided datasets for further analysis or validation purposes. For any inquiries related to the data or additional information, please contact the corresponding author.

**Acknowledgments:** We would like to thank the Fraunhofer Heinrich Hertz Institute for providing the FBG sensors. We also acknowledge the support by the Open Access Publishing Fund of Clausthal University of Technology.

**Conflicts of Interest:** The authors declare no conflicts of interest. The founders had no part in the design of the study; in the collection, analyses, or interpretation of data; in the writing of the manuscript, or in the decision to publish the results.

## Abbreviations

The following abbreviations are used in this manuscript:

CC	Constant Current
CV	Constant Voltage
DMC	Dimethyl Carbonate
EC	Ethylene Carbonate
FBG	Fiber Bragg Grating
FOI	Feature(s) Of Interest
ICA	Incremental Capacity Analysis
LAM	Loss of Active Material
LLI	Loss Lithium Inventory
ORI	Ohmic Resistance Increase
OSD	Over-charge Safety Device
PHEV	Plug-In Hybrid Electric Vehicle
SEI	Solid Electrolyte Interphase
SOC	State Of Charge
TR	Thermal Runaway

## Appendix A

### Appendix A.1. Experimental Results

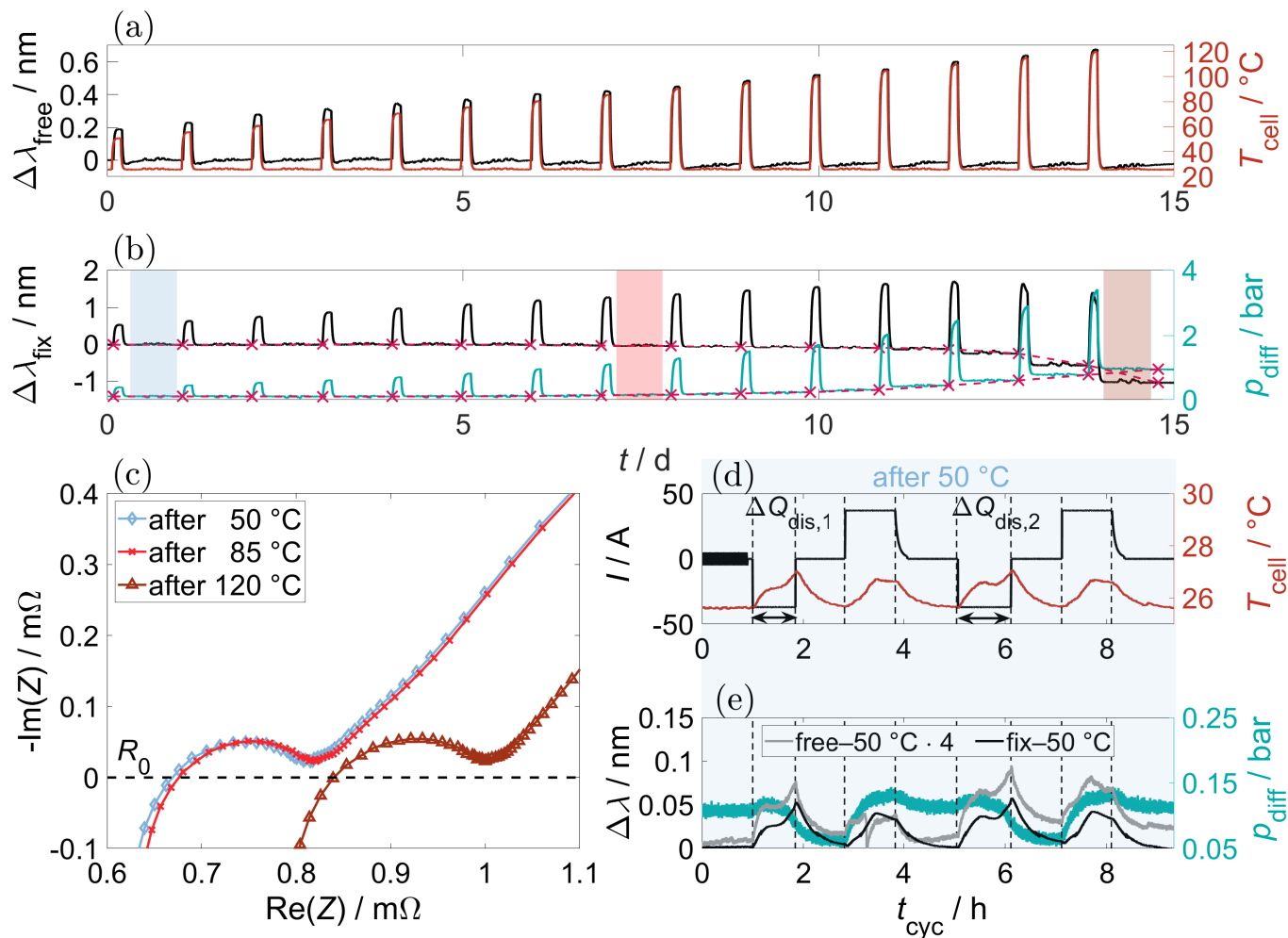


**Figure A1.** Overview of the results of experiment O1. (a): The free FBG wavelength change and temperature profile of the Pt100 sensor on top of the cell during test time. In comparison, the contact of the free FBG sensor with tape was realized worse than in the B1 experiment that led to less stable wavelength changes. (b): The progression of pressure and fixed FBG signals over the test duration and high-temperature phases with initial reversible changes to 70 °C and accumulating irreversible changes with increasing temperature. (c): Impedance spectroscopy spectra after 50, 85, and 120 °C temperature phases before a capacity determination at 25 °C. (d): Current profile for capacity determination and measured temperatures at 25 °C after the 50 °C phase. (e): Sensor performance of the pressure, as well as the free and fixed FBG sensor during cycling after 50 °C. The wavelength change of the free FBG sensor was multiplied by four to create a comparable signal level to the fixed FBG sensor.

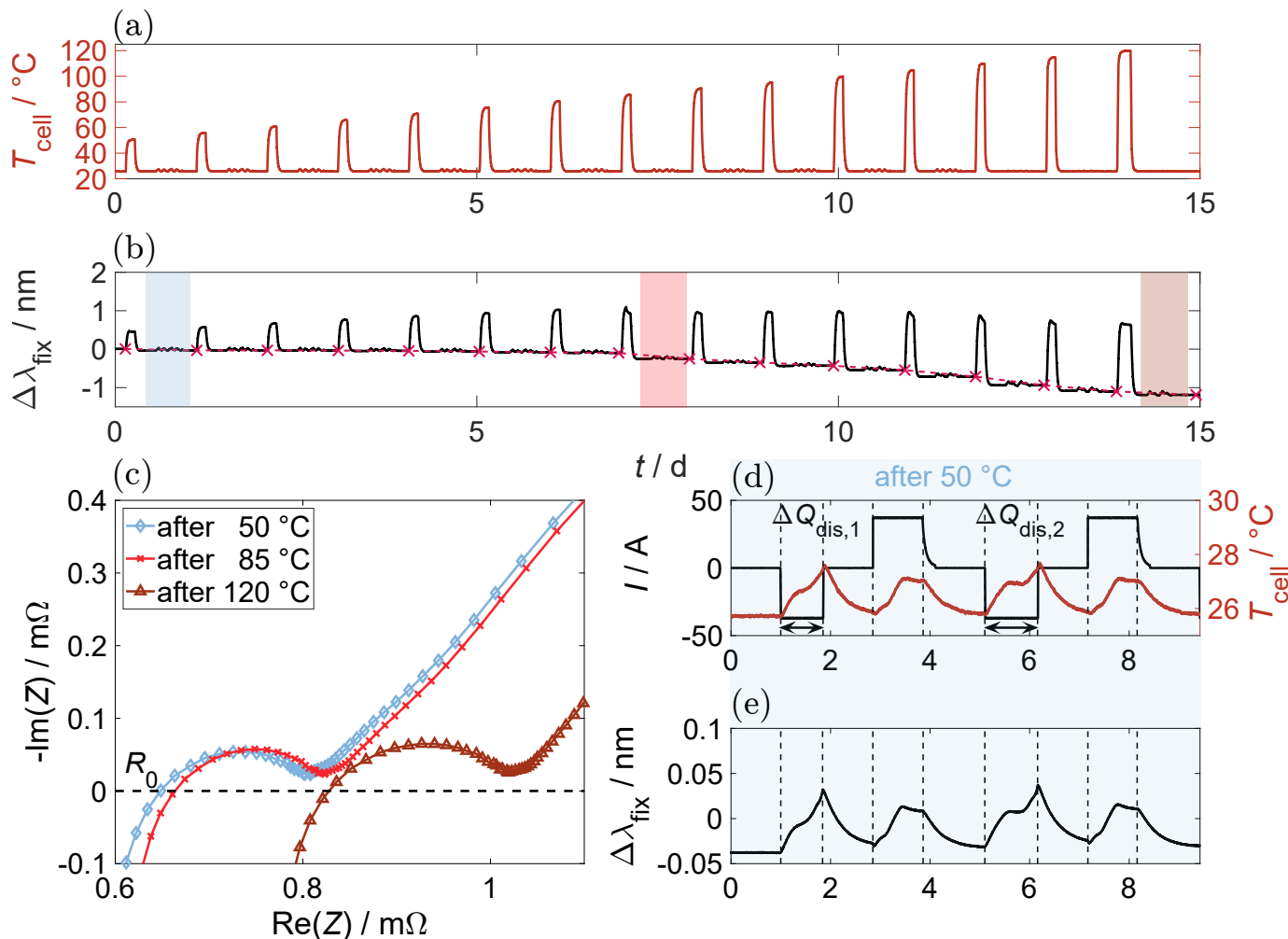


**Figure A2.** Overview of the results of experiment B2. **(a)**: Temperature profile of the Pt100 sensor on top of the cell during test time. Due to an error, the 120  $^\circ\text{C}$  rest was prolonged from the usual duration of 3 h to 4.5 h, and the contact loosening of the Pt100 sensor on top of the cell after 110  $^\circ\text{C}$ , which resulted in an insufficient temperature measurement during cycling. **(b)**: Progression of the fixed FBG signals over the test duration and high-temperature phases with initial reversible changes to 70  $^\circ\text{C}$ , as well as the accumulation of irreversible changes with increasing temperature. **(c)**: Impedance spectroscopy spectra after 50, 85, and 120  $^\circ\text{C}$  temperature phases before capacity determination at 25  $^\circ\text{C}$ . **(d)**: Current profile for capacity determination and the measured temperature at 25  $^\circ\text{C}$  after the 50  $^\circ\text{C}$  phase. **(e)**: Sensor performance of the fixed FBG sensor during cycling.

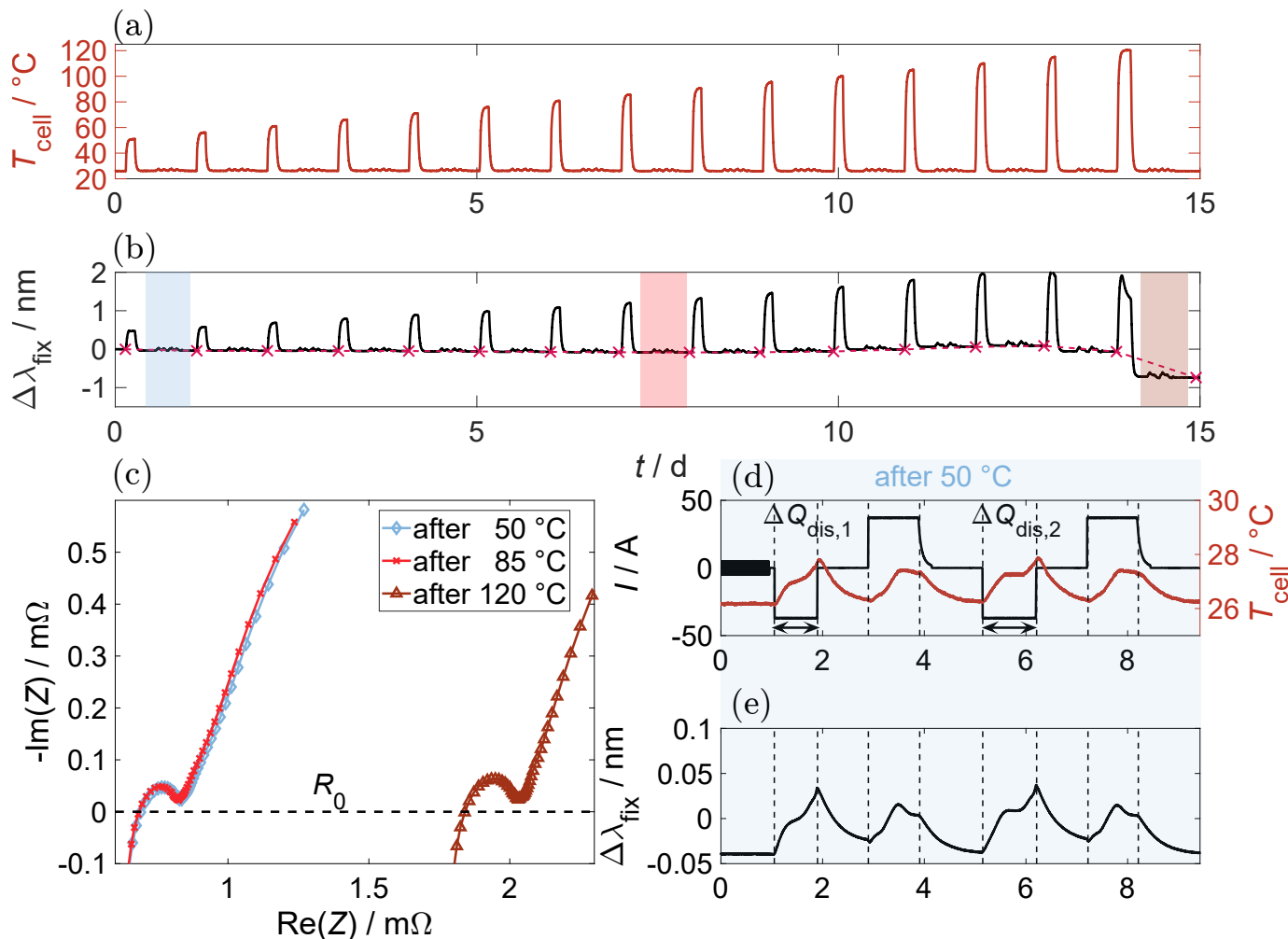


**Figure A3.** Overview of the results of experiment O2. (a): Temperature profile of the Pt100 sensor on top of the cell during test time. Due to an error, the 120 °C rest was prolonged from the usual duration of 3 h to 4.5 h. (b): Progression of the fixed FBG signal over the test duration and high-temperature phases with initial reversible changes to 70 °C, as well as the accumulation of irreversible changes with increasing temperature. (c): Impedance spectroscopy spectra after 50, 85, and 120 °C temperature phases before capacity determination at 25 °C. (d): Current profile for the capacity determination and measured temperature at 25 °C after the 50 °C phase. (e): Sensor performance of the fixed FBG sensor during cycling.

### Appendix A.2. Characteristic Trends

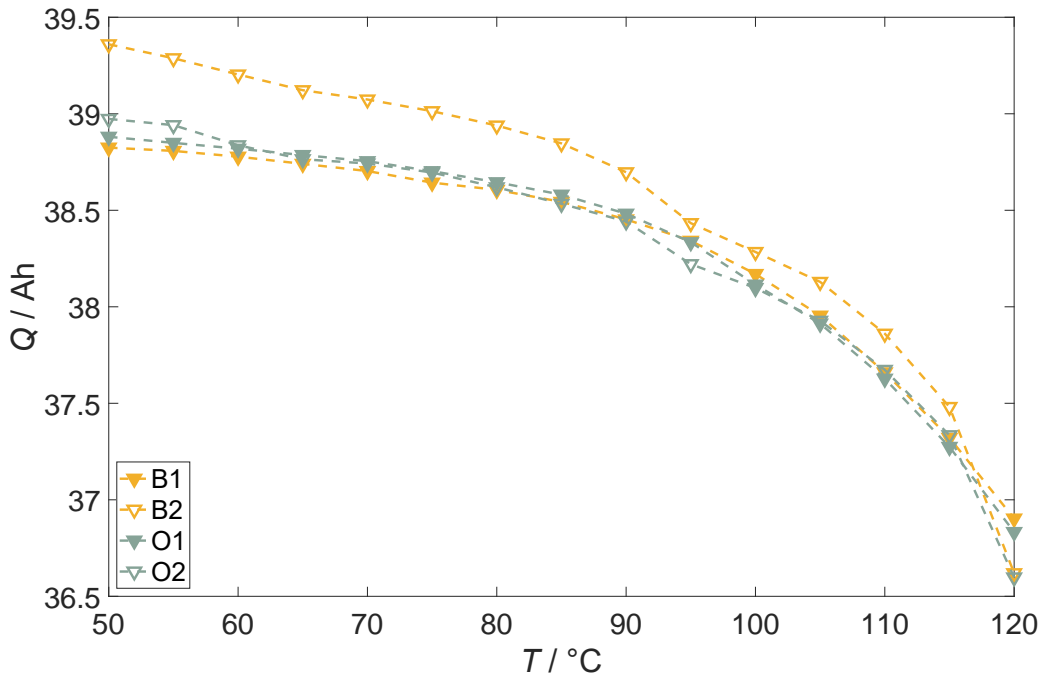


**Figure A4.** Decrease in the cell capacity at 25 °C after the high-temperature phase for each cell at the time before the start of the next high-temperature phase.

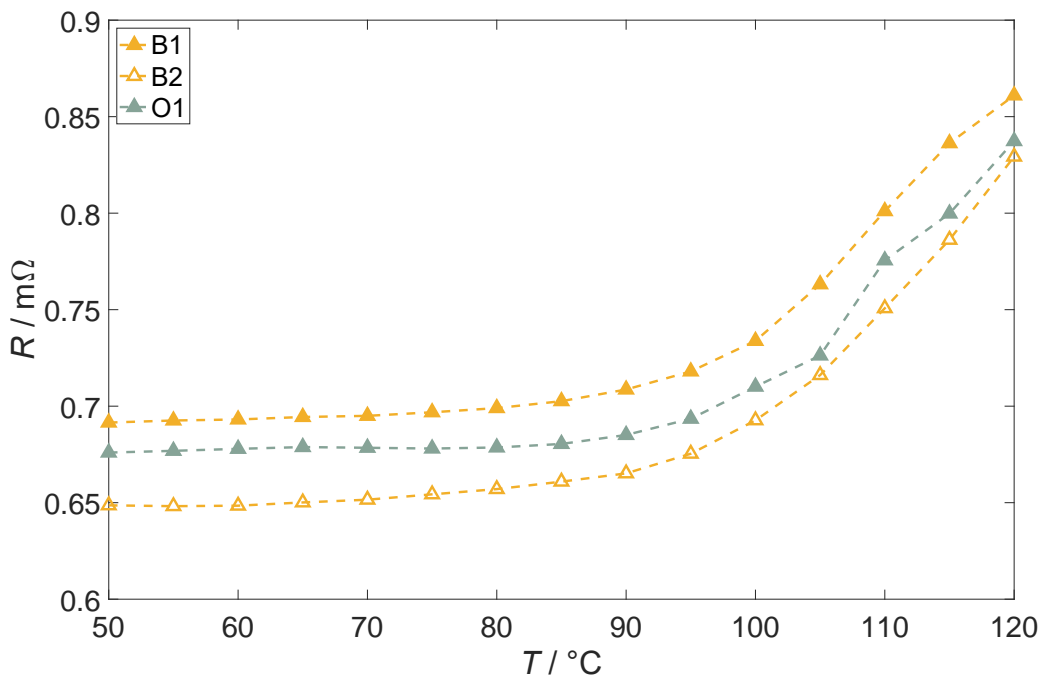


**Figure A5.** Increase in the Ohmic cell resistance at 25 °C after the high-temperature phase for each cell at the time before the start of the next high-temperature phase. The result of the O2 setup is not displayed due to an error during GEIS measurement.

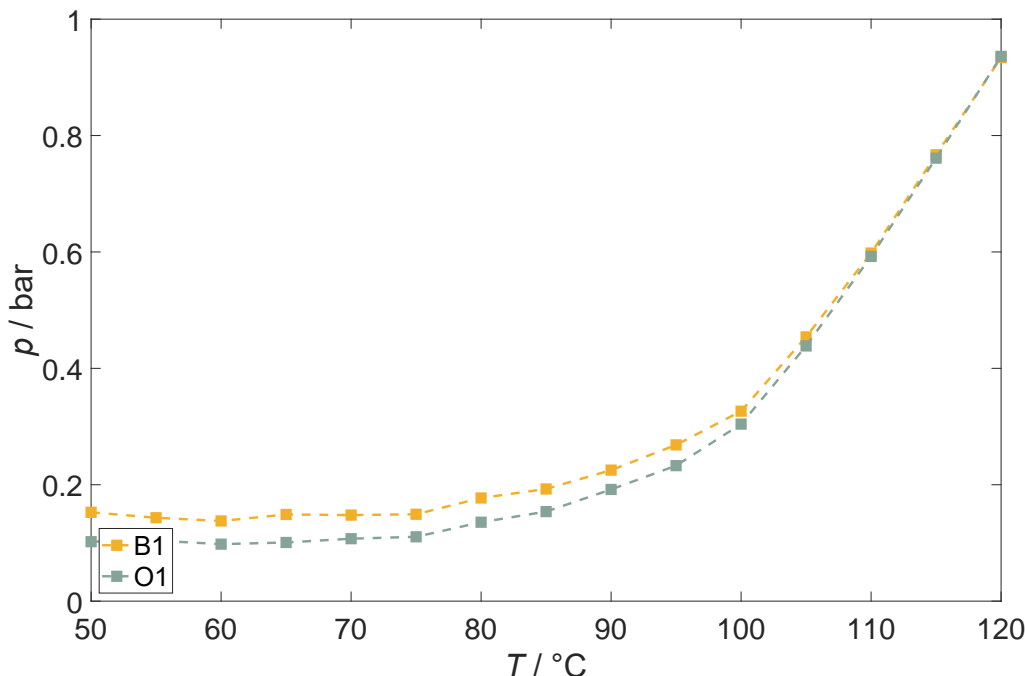


**Figure A6.** Increase in cell pressure at 25 °C after the high-temperature phase for each cell at rest before the start of the next high-temperature phase, as marked in Figures 7b and A1b.

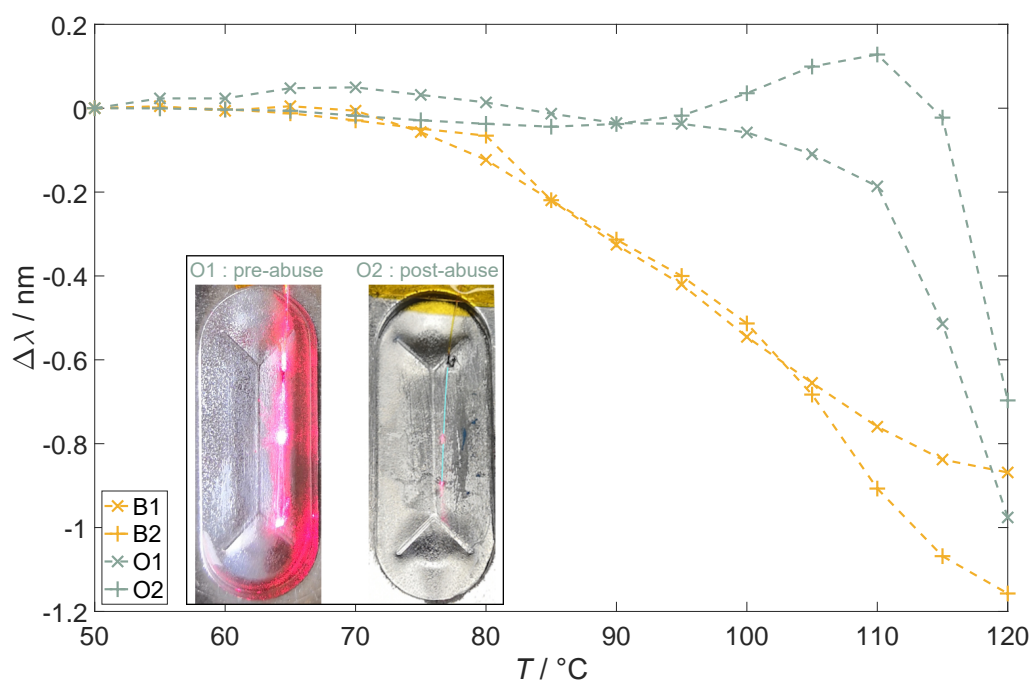


**Figure A7.** Change in the Bragg wavelength in the FBG sensor that was fixed on the rupture disc at 25 °C after the high-temperature phase for each cell at the time before the start of the next high-temperature phase relative to the measurement after the 50 °C phase. Inset picture of the fixed FBG position on the rupture disc for the experiments O1 (before abuse test) and O2 (after abuse test).

## References

1. Bhandari, N.; Cai, A.; Yuzawa, K.; Zhang, J.; Joshi, V.; Fang, F.; Lee, G.; Harada, R.; Shin, S. Batteries: The Greenflation Challenge. Available online: <https://www.goldmansachs.com/intelligence/pages/gs-research/batteries-the-greenflation-challenge/report.pdf> (accessed on 11 January 2024).
2. Degen, F.; Winter, M.; Bendig, D.; Tübke, J. Energy consumption of current and future production of lithium-ion and post lithium-ion battery cells. *Nat. Energy* **2023**, *8*, 1284–1295. [CrossRef]

3. Liu, W.; Placke, T.; Chau, K.T. Overview of batteries and battery management for electric vehicles. *Energy Rep.* **2022**, *8*, 4058–4084. [[CrossRef](#)]
4. Finegan, D.P.; Darcy, E.; Keyser, M.; Tjaden, B.; Heenan, T.M.M.; Jervis, R.; Bailey, J.J.; Malik, R.; Vo, N.T.; Magdysyuk, O.V.; et al. Characterising thermal runaway within lithium-ion cells by inducing and monitoring internal short circuits. *Energy Environ. Sci.* **2017**, *10*, 1377–1388. [[CrossRef](#)]
5. Chen, Y.; Kang, Y.; Zhao, Y.; Wang, L.; Liu, J.; Li, Y.; Liang, Z.; He, X.; Li, X.; Tavajohi, N.; et al. A review of lithium-ion battery safety concerns: The issues, strategies, and testing standards. *J. Energy Chem.* **2021**, *59*, 83–99. [[CrossRef](#)]
6. Finegan, D.P.; Darst, J.; Walker, W.; Li, Q.; Yang, C.; Jervis, R.; Heenan, T.M.; Hack, J.; Thomas, J.C.; Rack, A.; et al. Modelling and experiments to identify high-risk failure scenarios for testing the safety of lithium-ion cells. *J. Power Sources* **2019**, *417*, 29–41. [[CrossRef](#)]
7. Essl, C.; Golubkov, A.W.; Fuchs, A. Comparing Different Thermal Runaway Triggers for Two Automotive Lithium-Ion Battery Cell Types. *J. Electrochem. Soc.* **2020**, *167*, 130542. [[CrossRef](#)]
8. Grabow, J.; Klink, J.; Benger, R.; Hauer, I.; Beck, H.P. Particle Contamination in Commercial Lithium-Ion Cells—Risk Assessment with Focus on Internal Short Circuits and Replication by Currently Discussed Trigger Methods. *Batteries* **2023**, *9*, 9. [[CrossRef](#)]
9. Li, H.; Duan, Q.; Zhao, C.; Huang, Z.; Wang, Q. Experimental investigation on the thermal runaway and its propagation in the large format battery module with Li(Ni1/3Co1/3Mn1/3)O2 as cathode. *J. Hazard. Mater.* **2019**, *375*, 241–254. [[CrossRef](#)]
10. Cai, T. Detection of Lithium-Ion Battery Failure and Thermal Runaway. Ph.D. Thesis, The University of Michigan, Ann Arbor, MI, USA, 2021. [[CrossRef](#)]
11. Klink, J.; Grabow, J.; Orazov, N.; Benger, R.; Börger, A.; Ahlberg Tidblad, A.; Wenzl, H.; Beck, H.P. Thermal fault detection by changes in electrical behaviour in lithium-ion cells. *J. Power Sources* **2021**, *490*, 229572. [[CrossRef](#)]
12. Tran, M.K.; Mevawalla, A.; Aziz, A.; Panchal, S.; Xie, Y.; Fowler, M. A Review of Lithium-Ion Battery Thermal Runaway Modeling and Diagnosis Approaches. *Processes* **2022**, *10*, 1192. [[CrossRef](#)]
13. Klink, J.; Hebenbrock, A.; Grabow, J.; Orazov, N.; Nylén, U.; Benger, R.; Beck, H.P. Comparison of Model-Based and Sensor-Based Detection of Thermal Runaway in Li-Ion Battery Modules for Automotive Application. *Batteries* **2022**, *8*, 34. [[CrossRef](#)]
14. Zhang, Y.; Jiang, M.; Zhou, Y.; Zhao, S.; Yuan, Y. Towards High-Safety Lithium-Ion Battery Diagnosis Methods. *Batteries* **2023**, *9*, 63. [[CrossRef](#)]
15. Feng, X.; Ren, D.; He, X.; Ouyang, M. Mitigating Thermal Runaway of Lithium-Ion Batteries. *Joule* **2020**, *4*, 743–770. [[CrossRef](#)]
16. Li, A.; Yuen, A.C.Y.; Wang, W.; de Cachinho Cordeiro, I.M.; Wang, C.; Chen, T.B.Y.; Zhang, J.; Chan, Q.N.; Yeoh, G.H. A Review on Lithium-Ion Battery Separators towards Enhanced Safety Performances and Modelling Approaches. *Molecules* **2021**, *26*, 478. [[CrossRef](#)]
17. Zhang, J.; Shao, D.; Jiang, L.; Zhang, G.; Wu, H.; Day, R.; Jiang, W. Advanced thermal management system driven by phase change materials for power lithium-ion batteries: A review. *Renew. Sustain. Energy Rev.* **2022**, *159*, 112207. [[CrossRef](#)]
18. Qiu, M.; Liu, J.; Cong, B.; Cui, Y. Research Progress in Thermal Runaway Vent Gas Characteristics of Li-Ion Battery. *Batteries* **2023**, *9*, 411. [[CrossRef](#)]
19. Ruiz, V.; Pfarrang, A.; Kriston, A.; Omar, N.; van den Bossche, P.; Boon-Brett, L. A review of international abuse testing standards and regulations for lithium ion batteries in electric and hybrid electric vehicles. *Renew. Sustain. Energy Rev.* **2018**, *81*, 1427–1452. [[CrossRef](#)]
20. Regulation (EU) 2023/1542; Concerning Batteries and Waste Batteries, Amending Directive 2008/98/EC and Regulation (EU) 2019/1020 and Repealing Directive 2006/66/EC. European Parliament: Strasbourg, France, 2023.
21. Feng, X.; Ren, D.; Zhang, S.; He, X.; Wang, L.; Ouyang, M. Influence of aging paths on the thermal runaway features of lithium-ion batteries in accelerating rate calorimetry tests. *Int. J. Electrochem. Sci.* **2019**, *14*, 44–58. [[CrossRef](#)]
22. Yamaki, J. Thermal stability of graphite anode with electrolyte in lithium-ion cells. *Solid State Ion.* **2002**, *148*, 241–245. [[CrossRef](#)]
23. Spotnitz, R.; Franklin, J. Abuse behavior of high-power, lithium-ion cells. *J. Power Sources* **2003**, *113*, 81–100. [[CrossRef](#)]
24. Zheng, S.; Wang, L.; Feng, X.; He, X. Probing the heat sources during thermal runaway process by thermal analysis of different battery chemistries. *J. Power Sources* **2018**, *378*, 527–536. [[CrossRef](#)]
25. Schmidt, J.P. Verfahren zur Charakterisierung und Modellierung von Lithium-Ionen Zellen. Ph.D. Thesis, Karlsruhe Institute of Technology, Karlsruhe, Germany, 2013. [[CrossRef](#)]
26. Zhang, Y.; Wang, H.; Wang, Y.; Li, C.; Liu, Y.; Ouyang, M. Thermal abusive experimental research on the large-format lithium-ion battery using a buried dual-sensor. *J. Energy Storage* **2021**, *33*, 102156. [[CrossRef](#)]
27. Golubkov, A.W.; Fuchs, D.; Wagner, J.; Wiltsche, H.; Stangl, C.; Fauler, G.; Voitic, G.; Thaler, A.; Hacker, V. Thermal-runaway experiments on consumer Li-ion batteries with metal-oxide and olivine-type cathodes. *RSC Adv.* **2014**, *4*, 3633–3642. [[CrossRef](#)]
28. Wang, H.; Frisco, S.; Gottlieb, E.; Yuan, R.; Whitacre, J.F. Capacity degradation in commercial Li-ion cells: The effects of charge protocol and temperature. *J. Power Sources* **2019**, *426*, 67–73. [[CrossRef](#)]
29. Rowden, B.; Garcia-Araez, N. A review of gas evolution in lithium ion batteries. *Energy Rep.* **2020**, *6*, 10–18. [[CrossRef](#)]
30. Mattinen, U.; Klett, M.; Lindbergh, G.; Wreland Lindström, R. Gas evolution in commercial Li-ion battery cells measured by on-line mass spectrometry—Effects of C-rate and cell voltage. *J. Power Sources* **2020**, *477*, 228968. [[CrossRef](#)]
31. Feng, X.; Ouyang, M.; Liu, X.; Lu, L.; Xia, Y.; He, X. Thermal runaway mechanism of lithium ion battery for electric vehicles: A review. *Energy Storage Mater.* **2018**, *10*, 246–267. [[CrossRef](#)]

32. Zou, K.; Chen, X.; Ding, Z.; Gu, J.; Lu, S. Jet behavior of prismatic lithium-ion batteries during thermal runaway. *Appl. Therm. Eng.* **2020**, *179*, 115745. [\[CrossRef\]](#)
33. Cheng, A.; Xin, Y.; Wu, H.; Yang, L.; Deng, B. A Review of Sensor Applications in Electric Vehicle Thermal Management Systems. *Energies* **2023**, *16*, 5139. [\[CrossRef\]](#)
34. Popp, H.; Koller, M.; Jahn, M.; Bergmann, A. Mechanical methods for state determination of Lithium-Ion secondary batteries: A review. *J. Energy Storage* **2020**, *32*, 101859. [\[CrossRef\]](#)
35. Chen, D.; Zhao, Q.; Zheng, Y.; Xu, Y.; Chen, Y.; Ni, J.; Zhao, Y. Recent Progress in Lithium-Ion Battery Safety Monitoring Based on Fiber Bragg Grating Sensors. *Sensors* **2023**, *23*, 5609. [\[CrossRef\]](#)
36. Jia, T.; Zhang, Y.; Ma, C.; Li, S.; Yu, H.; Liu, G. The early warning for overcharge thermal runaway of lithium-ion batteries based on a composite parameter. *J. Power Sources* **2023**, *555*, 232393. [\[CrossRef\]](#)
37. Zhang, L.; Liu, X.; Li, K.; Du, D.; Zheng, M.; Niu, Q.; Yang, Y.; Zhou, Q.; Sun, T.; Grattan, K.T.V. Real-Time Battery Temperature Monitoring Using FBG Sensors: A Data-Driven Calibration Method. *IEEE Sens. J.* **2022**, *22*, 18639–18648. [\[CrossRef\]](#)
38. Liu, S.; Li, K. Thermal monitoring of lithium-ion batteries based on machine learning and fibre Bragg grating sensors. *Trans. Inst. Meas. Control.* **2023**, *45*, 1570–1578. [\[CrossRef\]](#)
39. Chang, L.; Chen, W.; Mao, Z.; Huang, X.; Ren, T.; Zhang, Y.; Cai, Z. Experimental study on the effect of ambient temperature and discharge rate on the temperature field of prismatic batteries. *J. Energy Storage* **2023**, *59*, 106577. [\[CrossRef\]](#)
40. Tardy, E.; Thivel, P.X.; Druart, F.; Kuntz, P.; Devaux, D.; Bultel, Y. Internal temperature distribution in lithium-ion battery cell and module based on a 3D electrothermal model: An investigation of real geometry, entropy change and thermal process. *J. Energy Storage* **2023**, *64*, 107090. [\[CrossRef\]](#)
41. DIN 91252:2016-11; Elektrische Straßenfahrzeuge—Batteriesysteme—Electrically Propelled Road Vehicles—Battery Systems—Design Specifications for Lithium-Ion Battery Cells. German Institute for Standardization: Berlin, Germany, 2016. [\[CrossRef\]](#)
42. Barai, A.; Tangirala, R.; Uddin, K.; Chevalier, J.; Guo, Y.; McGordon, A.; Jennings, P. The effect of external compressive loads on the cycle lifetime of lithium-ion pouch cells. *J. Energy Storage* **2017**, *13*, 211–219. [\[CrossRef\]](#)
43. Holland, A.A. The Effects of Compression on Lithium-Ion Batteries. Ph.D. Thesis, Imperial College London, London, UK, 2018. [\[CrossRef\]](#)
44. Kohlberger, M. Sicherheitselement für Batteriezelle. European Patent Office EP2779271A2, 21 January 2014.
45. Peled, E. The Electrochemical Behavior of Alkali and Alkaline Earth Metals in Nonaqueous Battery Systems—The Solid Electrolyte Interphase Model. *J. Electrochem. Soc.* **1979**, *126*, 2047–2051. [\[CrossRef\]](#)
46. Peled, E.; Menkin, S. Review—SEI: Past, Present and Future. *J. Electrochem. Soc.* **2017**, *164*, A1703–A1719. [\[CrossRef\]](#)
47. Pinson, M.B.; Bazant, M.Z. Theory of SEI Formation in Rechargeable Batteries: Capacity Fade, Accelerated Aging and Lifetime Prediction. *J. Electrochem. Soc.* **2013**, *160*, A243–A250. [\[CrossRef\]](#)
48. Son, K.; Hwang, S.M.; Woo, S.G.; Paik, M.; Song, E.H.; Kim, Y.J. Thermal and chemical characterization of the solid-electrolyte interphase in Li-ion batteries using a novel separator sampling method. *J. Power Sources* **2019**, *440*, 227083. [\[CrossRef\]](#)
49. Chen, S.; Gao, Z.; Sun, T. Safety challenges and safety measures of Li-ion batteries. *Energy Sci. Eng.* **2021**, *9*, 1647–1672. [\[CrossRef\]](#)
50. Aurbach, D.; Ein-Eli, Y.; Markovsky, B.; Zaban, A.; Luski, S.; Carmeli, Y.; Yamin, H. The Study of Electrolyte Solutions Based on Ethylene and Diethyl Carbonates for Rechargeable Li Batteries: II. Graphite Electrodes. *J. Electrochem. Soc.* **1995**, *142*, 2882–2890. [\[CrossRef\]](#)
51. Tanaka, N. Modeling and Simulation of Thermo-Electrochemistry of Thermal Runaway in Lithium-Ion Batteries. Ph.D. Thesis, University of Stuttgart, Stuttgart, Germany, 2015. [\[CrossRef\]](#)
52. Richard, M.N.; Dahn, J.R. Accelerating Rate Calorimetry Study on the Thermal Stability of Lithium Intercalated Graphite in Electrolyte. I. Experimental. *J. Electrochem. Soc.* **1999**, *146*, 2068–2077. [\[CrossRef\]](#)
53. Wang, Q.; Sun, J.; Yao, X.; Chen, C. Thermal stability of LiPF6/EC+DEC electrolyte with charged electrodes for lithium ion batteries. *Thermochim. Acta* **2005**, *437*, 12–16. [\[CrossRef\]](#)
54. Deshpande, R.D.; Bernardi, D.M. Modeling Solid-Electrolyte Interphase (SEI) Fracture: Coupled Mechanical/Chemical Degradation of the Lithium Ion Battery. *J. Electrochem. Soc.* **2017**, *164*, A461–A474. [\[CrossRef\]](#)
55. Palacín, M.R.; de Guibert, A. Why do batteries fail? *Science* **2016**, *351*, 1253292. [\[CrossRef\]](#)
56. Zhou, M.; Zhao, L.; Okada, S.; Yamaki, J.I. Quantitative Studies on the Influence of LiPF 6 on the Thermal Stability of Graphite with Electrolyte. *J. Electrochem. Soc.* **2011**, *159*, A44–A48. [\[CrossRef\]](#)
57. Agubra, V.A.; Fergus, J.W. The formation and stability of the solid electrolyte interface on the graphite anode. *J. Power Sources* **2014**, *268*, 153–162. [\[CrossRef\]](#)
58. Carter, R.; Kingston, T.A.; Atkinson, R.W.; Parmananda, M.; Dubarry, M.; Fear, C.; Mukherjee, P.P.; Love, C.T. Directionality of thermal gradients in lithium-ion batteries dictates diverging degradation modes. *Cell Rep. Phys. Sci.* **2021**, *2*, 100351. [\[CrossRef\]](#)
59. Dubarry, M.; Anseán, D. Best practices for incremental capacity analysis. *Front. Energy Res.* **2022**, *10*, 1023555. [\[CrossRef\]](#)
60. Schmitt, J.; Kraft, B.; Schmidt, J.P.; Meir, B.; Elian, K.; Ensling, D.; Keser, G.; Jossen, A. Measurement of gas pressure inside large-format prismatic lithium-ion cells during operation and cycle aging. *J. Power Sources* **2020**, *478*, 228661. [\[CrossRef\]](#)
61. Werneck, M.M.; Allil, R.C.S.B.; Ribeiro, B.A.; de Nazaré, F.V.B. A Guide to Fiber Bragg Grating Sensors. In *Current Trends in Short-and Long-Period Fiber Gratings*; Cuadrado-Laborde, C., Ed.; InTech: London, UK, 2013. [\[CrossRef\]](#)
62. Sahota, J.K.; Gupta, N.; Dhawan, D. Fiber Bragg grating sensors for monitoring of physical parameters: A comprehensive review. *Opt. Eng.* **2020**, *59*, 060901. [\[CrossRef\]](#)

63. Schlueter, V.G. Entwicklung Eines Experimentell Gestützten Bewertungsverfahrens zur Optimierung und Charakterisierung der Dehnungsübertragung Oberflächenapplizierter Faser-Bragg-Gitter-Sensoren. Ph.D. Thesis, Technische Universität Berlin, Berlin, Germany, 2009.
64. Wan, K.T.; Leung, C.K.Y.; Olson, N.G. Investigation of the strain transfer for surface-attached optical fiber strain sensors. *Smart Mater. Struct.* **2008**, *17*, 035037. [[CrossRef](#)]
65. Barai, A.; Uddin, K.; Dubarry, M.; Somerville, L.; McGordon, A.; Jennings, P.; Bloom, I. A comparison of methodologies for the non-invasive characterisation of commercial Li-ion cells. *Prog. Energy Combust. Sci.* **2019**, *72*, 1–31. [[CrossRef](#)]
66. Matasso, A.; Wetz, D.; Liu, F. The Effects of Internal Pressure Evolution on the Aging of Commercial Li-Ion Cells. *J. Electrochem. Soc.* **2015**, *162*, A92–A97. [[CrossRef](#)]
67. Schweidler, S.; de Biasi, L.; Schiele, A.; Hartmann, P.; Brezesinski, T.; Janek, J. Volume Changes of Graphite Anodes Revisited: A Combined Operando X-ray Diffraction and In Situ Pressure Analysis Study. *J. Phys. Chem. C* **2018**, *122*, 8829–8835. [[CrossRef](#)]
68. Ansean, D.; Gonzalez, M.; Blanco, C.; Viera, J.C.; Fernandez, Y.; Garcia, V.M. Lithium-ion battery degradation indicators via incremental capacity analysis. In Proceedings of the 2017 IEEE International Conference on Environment and Electrical Engineering and 2017 IEEE Industrial and Commercial Power Systems Europe (EEEIC/I&CPS Europe), Milan, Italy, 6–9 June 2017; pp. 1–6. [[CrossRef](#)]
69. Feng, X.; Sun, J.; Ouyang, M.; He, X.; Lu, L.; Han, X.; Fang, M.; Peng, H. Characterization of large format lithium ion battery exposed to extremely high temperature. *J. Power Sources* **2014**, *272*, 457–467. [[CrossRef](#)]
70. Birk, C.R.; Roberts, M.R.; McTurk, E.; Bruce, P.G.; Howey, D.A. Degradation diagnostics for lithium ion cells. *J. Power Sources* **2017**, *341*, 373–386. [[CrossRef](#)]

**Disclaimer/Publisher's Note:** The statements, opinions and data contained in all publications are solely those of the individual author(s) and contributor(s) and not of MDPI and/or the editor(s). MDPI and/or the editor(s) disclaim responsibility for any injury to people or property resulting from any ideas, methods, instructions or products referred to in the content.